NANOPORES AS VOLUMETRIC STORAGE UNITS IN OVER-PRESSURED SOURCE ROCKS

A Thesis

by

MOJOOLAOLU GBOLABO MALOMO

Submitted to the Graduate and Professional School of
Texas A&M University
in partial fulfillment of the requirements for the degree of

MASTER OF SCIENCE

Chair of Committee,	I. Yucel Akkutlu
Committee Members,	W. John Lee
	Benchun Duan
Head of Department,	Jeff Spath

December 2021

Major Subject: Petroleum Engineering

ABSTRACT

In this thesis, the fluid storage capacity of organic nanopores, as part of an over-pressured source-rock reservoir system, is investigated using a molecular simulation approach. The results indicate that organic nanopores at high pressure and high temperature subsurface environment behave as volumetric storage units, contributing to the total hydrocarbon in-place. In cases where these nanopores are part of the effective pore network, these pores feed into the fracture network and have the potential to increase recovery. This volumetric behavior is different than the previous studies that showed nanoconfinement effects leading to trapping of the hydrocarbons, hence a reduction in the effective porosity.

DEDICATION

To my wife, Fifunmi, whose passion to see me finish this work was probably greater than mine.

ACKNOWLEDGEMENTS

My committee chair, Dr. Akkutlu, was an immense pillar throughout the course of this research. He was especially patient and kind; and his excitement about the results was infectious. Thank you, sir.

To my committee members, Dr. Lee and Dr. Duan, I say thank you for your kind and constructive feedback. It was a pleasure to be taught by you.

My sincerest gratitude also goes to Dr. Seunghwan Baek ’19. His dissertation work and guidance were invaluable for this study, especially at the early stages.

Finally, a big thanks to my friends and colleagues, especially those in the Department of Petroleum Engineering at Texas A&M University. It was good to know, and be known by you all.

CONTRIBUTORS AND FUNDING SOURCES

Contributors

This study was supervised by a thesis committee consisting of Professors I. Y. Akkutlu (chair) and W. J. Lee, both in the Department of Petroleum Engineering, and Professor B. Duan from Geology and Geophysics.

Funding

This research was funded by the Graduate Assistantship in the Department of Petroleum Engineering at Texas A&M University.

NOMENCLATURE

a	Dimensionless coefficient
b	Dimensionless coefficient
B_g	Gas formation volume factor
B_g^*	Modified gas formation volume factor
c	Dimensionless coefficient
CE	Confinement effect
d	Dimensionless coefficient
d_p	Pore size
$d_{p,L}$	Cut-off pore size for nanopore confinement effects
E_{angle}	Angle potential
E_{bond}	Bond potential
E_{bonded}	Energy from covalent bonds
$E_{dihedral}$	Dihedral potential
$E_{electrostatic}$	Electrostatic energy
$E_{nonbonded}$	Energy from non-covalent bonds
E_{total}	Total potential energy
$E_{vanderWaals}$	Van der Waals potential
$f(v_i)$	Velocity function
$G^*(p)$	Gas in place with nanopore confinement effects

$G_{s,i}$	Amount of component i in sorbed phase
G_s	Adsorbed gas in place
G_f	Free gas in place
G_{sL}	Langmuir volume
G_{sLi}	Langmuir volume of gas component i
G_{total}	Total shale gas in place
k_B	Boltzmann's constant
k_{angles}	Angle force constant
k_{bonds}	Bond force constant
$k_{dihedrals}$	Dihedral force constant
l	Bond length
l_o	Equilibrium bond length
m	Mass
$\widehat{M}$	Apparent natural gas molecular weight
n	Periodic parameter
n_b	Number density of fluid in the bulk phase
n_{d_p}	Number density of fluid in pore of size d_p
N	Number of molecules
N_f	Number of degrees of freedom
p	Pressure
p_L	Langmuir pressure

p_{Li}	Langmuir pressure of gas component i
p_d	Dew pressure
p_v	Vapor pressure
q_i	Atomic charge on molecule i
r_c	Cut-off distance beyond which intermolecular potential is 0
r_{cp}	Critical pore size to capillary condensation to occur
r_{ij}	Intermolecular distance between two particles/molecules
r_n	Neighbor list radius
s_o	Oil saturation
s_w	Water saturation
t	Time
T	Temperature
R	Gas constant
v_α	Average velocity
$V_{\%,dp}$	Pore volume percentage of nanopores of size d_p
V_L	Liquid molar density
V_l	Liquid volume
V_p	Effective hydrocarbon pore volume
V_{vl}	Mixture volume
x	Liquid molar composition
X	Ratio of p_v and p_d
y	Vapor molar composition

y_i	Gas phase mole fraction of component i
y_i	Vapor molar composition of component i
z	Gas compressibility factor
Z_{av}	Function of gas compressibility factor at p_v and p_d
θ_o	Equilibrium bond angle
ρ_b	Bulk rock density
ρ_{bulk,CH_4}	Bulk mass density of CH_4
$\rho_{bulk,mix}$	Bulk mass density of fluid
ρ_{bulk,mol,CH_4}	Bulk molar density of CH_4
$\rho_{bulk,mol}$	Bulk molar density of fluid
ρ_{dp,CH_4}	Mass density of CH_4 in nanopore of size d_p
$\rho_{dp,mix}$	Mass density of fluid in nanopore of size d_p
ρ_{dp,mol,CH_4}	Bulk molar density of CH_4 in nanopore of size d_p
$\rho_{dp,mol}$	Bulk molar density of fluid in nanopore of size d_p
ρ_s	Density of gas in sorbed phase
ϵ_0	Permittivity of free space
ϕ_s	Sorbed phase porosity fraction
$\phi_{inorganic}$	Inorganic porosity fraction
$\phi_{organic}$	Organic porosity fraction
$\Delta G_{a,i}$	Amount of component i desorbed
Δp	Pressure change

Δr	Arbitrary small distance
γ	Phase parameter
θ	Angle of contact
θ	Bond angle
λ	Surface Tension
σ	Distance between two molecules at which interaction energy is 0
υ	Volume fraction of large pores
ω	Dihedral bond torsion angle
ϵ	Well depth
ϕ	Porosity

TABLE OF CONTENTS

Page

LIST OF FIGURES

Page

LIST OF TABLES

Page

1. INTRODUCTION

1.1. Overview of Unconventional Reservoirs

With the advent of hydraulic fracturing technology in the oil and gas industry, the focus of hydrocarbon production has shifted significantly from conventional reservoirs to the unconventionals. The unconventional reservoirs are predominantly shale formations – sedimentary rocks with more than 50% of their grains smaller than 65 micrometers. (Potter et al. 2004). In general, shales have high clay content; the resource shales that are targeted for drilling and fracturing are often marine deposited siliceous shales predominantly constituting quartz, feldspars, carbonate, dolomite, pyrite etc. Hence, they could have complex lithology and pore structure. (Ilgen et al. 2017). They have characteristically low porosity and ultra-low permeability.

Resource shales are formed by the deposition of sediments, usually in deep and shallow lacustrine/marine environments. The deposited sediments are buried and compacted – mostly under the influence of gravity – and are subjected to high pressure and temperature. (Arthur and Sageman 1994).

In addition to the high clay content and varying inorganic mineral composition, shales that are source rocks also contain organic matter. Organic matter constitutes a small portion of the shale formation – usually about 5% of the shale mass and 10% of the shale volume. (Ilgen et al. 2017, Loucks et al. 2012). The former is also known as the Total Organic Carbon (TOC) of the shale. Shale formations of economic interest have TOC larger than 2%.

During the geological evolution of the formation, organic material is deposited as biomass together with the inorganic constituents and, during the burial and diagenesis processes, is metamorphosed into intermediate organic products such as kerogen and bitumen. Kerogen is a solid organic material, insoluble in organic solvents, formed from the break-down of biomass by aerobic bacterial activity in oxidizing environments (Tucker 2001), or from thermal break-down in anaerobic (reducing) environments. These are referred to as biogenic and thermogenic kerogen, respectively. The process of bitumen formation is also part of the rock's diagenesis. Some shales with particular biomass deposits could yield bitumen (a semi-liquid) organic mass. The maturity (the level of heat the organic material is exposed to during the thermal breakdown) of the organic material, and the amount of kerogen could play an important role in the formation of bitumen in shale. Shale formations that contain a significant amount of kerogen and bitumen are termed 'organic-rich' shale, or resource shale. In this study, the focus will be on high maturity resource shales that contain significant amount of kerogen (TOC higher than 2%), ignoring the added complexities that could appear due to presence of bitumen in the shale. Focused ion beam and scanning electron microscope images reveal that significant amounts of these mature kerogen are finely dispersed in the inorganic matrix of resource shale formations. (Loucks et al. 2009).

At sufficiently high temperatures, kerogen is broken down to form hydrocarbon fluids such as oil, condensate and gas through the physical and chemical processes of catagenesis. The heat required for the conversion of kerogen into petroleum is usually supplied by the heat flux from the mantle, by hydrothermal heating and, to a lesser extent,

by the radioactive decay taking place in the formation. The hydrocarbon fluids generated could range from the simplest molecule – methane (CH_4), with molecular weight 16.04 g/mol – to the most complex asphaltene colloids that have molecular weights in the thousands. (Tucker 2001).

The generated hydrocarbon fluids form the organic pores. In high maturity source rocks kerogen pores can be identified with the scanning electron microscopy, whereas in other formations, pores are also observed in solid bitumen. In addition to these organic pores, with increasing pore pressures, the generated fluids create other secondary porosity features such as micro-cracks and fractures. So, when the resource shale is discovered and wells are drilled, production operations target fluids that are stored, not only as a part of the tight shale matrix (made up of the inter-particle porosity) but also those stored in the fractures and micro-cracks, and the organic pores. During oil and gas production, the fluids are transported via a multi-scale and complex network of pores and fractures that are hydraulically communicating with the well. (Loucks et al. 2012, Kou et al. 2016).

1.2. Hydrocarbon In Place Estimation

The hydrocarbon fluids are stored in different thermodynamic states in the resource shale formation as: (i) free fluid, (ii) adsorbed fluid, and (iii) absorbed or dissolved fluid. The large pores, micro-cracks and fractures mainly hold the free fluid molecules. The larger the pore volume and the higher the pore pressure, the larger the volume of free fluid stored. In this thesis, these large pore units will be referred to as volumetric storage units. The conventional oil and gas reservoirs store the hydrocarbon fluids this way, based on their available pore volume and the amount of overpressure.

Occasionally, this free fluid is referred to as compressed gas in the natural gas production engineering literature. The thermodynamic behavior of this natural gas can be predicted using the so-called compressibility equation of state. For example, the compressed natural gas density (ρ) can be determined accurately at a particular reservoir pressure and temperature (P and T, respectively) using the equation in the following form: $PM = z\rho RT$. There are several other equations of state such as van der Waals equation, or Peng-Robinson equation, that can also be used for the same purpose.

Unconventional resources also hold fluids volumetrically in large pores, micro-cracks and fractures. These resources (such as shales), as earlier discussed, are often rich in organic constituent. In organic-rich shale formations, the organic pores are orders of magnitude smaller than the micro-cracks and fractures. The organic pores have sizes that could vary from 100 nanometers (nm) down to the sizes of macromolecular openings that are less than 1 nm. Although organic pores are characteristically small, with small pore volume contribution to the storage, their walls have a large surface area. These walls are locations for the physical adsorption of hydrocarbon fluid molecules. Consequently, although the organic pores are not considered as volumetric fluid storage units, they experience significant physical adsorption as an alternative reservoir fluid storage mechanism. The adsorbed phase storage develops and become significant at high pore pressure when the walls of the organic pores exert strong attractive forces on the fluid molecules contained inside the pore. This causes the fluid molecules to adhere to the walls in an adsorbed state. Hence, the amount of fluid adsorbed in the small organic pores (i.e., nanopores) is not a measure of the pore volume, but of the available surface area of the

pore walls. The fluids at the center of the nanopores are not greatly influenced by the attractive forces of the pore walls and they remain as free molecules.

Absorption, on the other hand, develops at the small end of the organic nanopore size distribution. When the strong attraction between the pore walls and fluid molecules develops in micropores (with pore sizes less than 2 nm), then all the fluid molecules are under the influence of the walls and no free molecules exist in the pore. In this scenario, the fluid storage becomes volumetric again even though the surface forces are vigorously acting on the fluid molecules. During the laboratory measurements of fluid storage capacity of the organic-rich shale samples, no technology exists to separate the amount of absorbed fluid from the amount of adsorbed fluid. Hence, both are collectively termed the 'sorbed' fluid. In essence, the sorbed fluid is the fluid molecules adsorbed by the pore walls plus the fluid molecules dissolved in the solid kerogen.

The sorption mode of hydrocarbon storage in organic shale nanopores causes the thermodynamic behavior of the fluids to deviate from the compressed free fluid behavior. For example, the density of the fluid could be significantly greater in the organic nanopores. Furthermore, the fluid density could be a function of the pore size. This anomaly in the density of the fluids in nanopores is widely known in micro-fluidics and nano-fluidics, but the recognition of its significance on the volumetric hydrocarbon in-place calculations goes back to Ambrose et al. (2012). This complexity of fluid storage as a function of the organic pore size distribution makes the traditional volumetric methods of hydrocarbon in place estimation using porosity and saturations inappropriate for organic-rich shale formations.

To estimate the shale gas in place, assuming a natural gas that is mainly methane in the reservoir, Ambrose et al. (2012) accounted for the free gas volume G_f and the sorbed gas G_s:

$$G_{total} = G_f + G_s \quad \text{..... (1)}$$

The sorbed gas amount in the organic pores was modeled adopting the Langmuir isotherm, given as:

$$G_s = G_{sL} \frac{p}{p+p_L} \quad \text{..... (2)}$$

Under the traditional volumetric method, the free gas is modeled as a function of the gas pore volume, i.e., the pore volume taken by the gas phase:

$$G_f = 32.0368 \frac{\phi(1-s_w-s_o)}{\rho_b B_g} \quad \text{..... (3)}$$

Equation (3) is widely known and practiced in the industry. However, it does not account for the pore volume lost to the sorbed gas molecules. Ambrose et al. (2012) pointed out that, because shales have relatively small pore volume available for free gas storage and the sorption could be significant in these rocks, then the sorbed phase developing in the organic portion of that pore volume could have the potential to reduce the total pore volume. If the total pore volume is measured in the laboratory using the standard API method based on helium gas expansion into the pore network of the shale sample, because the amount measured does not include the sorption effect, the pore volume will be the total volume.

Ambrose et al. (2012) estimated the fractional volume of that total pore space occupied by the sorbed phase in terms of the sorbed phase porosity ϕ_s as:

$$\phi_s = 1.318 \times 10^{-6} \widehat{M} \frac{\rho_b}{\rho_s} \left[G_{sL} \frac{p}{p+p_L} \right] \quad (4)$$

Assuming the liquid hydrocarbon saturation in the formation is negligible, and taking equation (4) into account, Ambrose et al. (2012) estimated a reduced or corrected volume of free gas to be:

$$G_f = \frac{32.0368}{B_g} \left[\frac{\phi(1-s_w)}{\rho_b} - \frac{1.318 \times 10^{-6} \widehat{M}}{\rho_s} \left[G_{sL} \frac{p}{p+p_L} \right] \right] \quad (5)$$

Hence, the total gas-in-place for a one-component gas reservoir is given by combining equations (2) and (5) into equation (1):

$$G_{total} = \frac{32.0368}{B_g} \left[\frac{\phi(1-s_w)}{\rho_b} - \frac{1.318 \times 10^{-6} \widehat{M}}{\rho_s} \left[G_{sL} \frac{p}{p+p_L} \right] \right] + G_{sL} \frac{p}{p+p_L} \quad (6)$$

In reality, even though we have such methane-rich shale gas reservoir systems, the shale reservoirs could be multi-component systems. To account for these compositional effects, Ambrose et al. (2011) adopted the extended Langmuir model to account for the adsorbed gas:

$$G_s = \sum_{i=1}^{n} G_{sLi} \frac{y_i p}{p_{Li} \left[1 + \sum_{j=1}^{n} y_j \frac{p}{p_{Lj}} \right]} \quad (7)$$

Hence, for multi-component shale gas reservoir systems, considering the pore volume lost to the sorbed phase, the total gas in place is given as:

$$G_{total} = \frac{32.0368}{B_g} \left[\frac{\phi(1-s_w)}{\rho_b} - \frac{1.318 \times 10^{-6} \widehat{M}}{\rho_{s,mix}} \left[\sum_{i=1}^{n} G_{sLi} \frac{y_i p}{p_{Li} \left[1 + \sum_{j=1}^{n} y_j \frac{p}{p_{Lj}} \right]} \right] \right] +$$

$$\sum_{i=1}^{n} G_{sLi} \frac{y_i p}{p_{Li} \left[1 + \sum_{j=1}^{n} y_j \frac{p}{p_{Lj}} \right]} \quad (8)$$

By taking the pore volume lost to the adsorbed phase into account (instead of using the old volumetric method) while calculating the gas in place for a multi-component system, Das et al. (2012) reported that the old volumetric method overestimates the gas in place calculation by as much as 15%. Ambrose et al. (2012) showed, in their original work, that, depending on the TOC of the shale gas formations, the error could be even higher. (Their calculations showed a 33% decrease in the free gas storage capacity of an organic-rich shale).

Tolbert and Wu (2015) argued that the Langmuir model, although computationally undemanding, is limited in its ability to estimate the amount of sorbed hydrocarbons in the organic nanopores. One of their arguments is that the Langmuir model does not account for the interaction between the adsorbed fluid molecules and the pore walls. To overcome this limitation, they adopted a Simplified Density Model (SLD) approach, which predicts adsorption based on a cubic equation of state. Tolbert and Wu (2015) adopted a conceptual framework that associates the free gas volume only with the inorganic pore space, and the adsorbed gas volume only with the organic pore space. This framework is erroneous in that significant free gas can exist in the organic pore space, and some measure of adsorption can exist in the inorganic pore space. This is especially the case when the reservoir holds the fluids at high pore pressure. Equations (9) and (10) shows their approach for the free and sorbed gas in-place calculations, respectively:

$$G_f = 32.0368 \frac{\phi_{inorganic}(1-s_w)}{\rho_b B_g} \quad (9)$$

$$G_s = 32.0368 \frac{\phi_{organic}(1-s_w)}{\rho_b B_g} \quad (10)$$

Adopting equations (9) and (10) in calculating the total gas in place, Tolbert and Wu (2015) showed that their model predicts storage capacity values similar to the Ambrose model for pressures below 7000 psi. However, equation (10) estimates a much higher adsorbed gas capacity than the Langmuir model – the difference between both adsorption models was as high as 800% at 10,000 psi. Hence, due to their framework, Tolbert and Wu (2015) over-predicted the adsorbed gas amount, and under-predicted the free gas amount.

Probabilistic (Richardson and Yu 2018) and material balance equation approaches (Orozco and Aguilera 2016) have also been utilized in estimating hydrocarbon in place for unconventional reservoirs.

1.3. Fluid Composition

1.3.1. Pure Fluids

For single-component systems, the density of the fluid is highest by the pore walls of the organic nanopore, where adsorption occurs. Ambrose et al. (2012) adopted Langmuir's model – which assumes that the adsorption layer is one molecule thick – on nanopores charged with methane; and used molecular simulation to determine the density of the fluid at the wall. Their findings suggested that the fluid density at the walls is higher than the density of the fluid in the liquid phase.

Ambrose et al. (2012) also investigated the effects of pore-size and temperature on methane adsorption. They found that smaller pore sizes yield higher density adsorbates, and larger pore sizes leave room for more free gas at the center of the pores. Also, the hotter the system, the lower the density of the adsorbate.

Their results were corroborated by Al Ismail and Horne (2014) who reported that at pore widths above 10 nm, the density of methane becomes comparable with that in the bulk state. Feng and Akkutlu (2015) and Riewchotisakul and Akkutlu (2016) also arrived at similar results. In their own studies, they also investigated the effects of pore pressure on the density profile of the methane molecules in the pore. They reported that the overall density profile across the cross section of the pore increases with pressure. The increase was more pronounced for free fluid residing in the central portion of the pore and obeyed the compressibility equation of state.

Upon production, the free gas at the center of the pores escapes the pores and migrate towards the hydraulic fractures of the well. As the pore pressure is reduced, some of the adsorbed gas by the pore walls are released, or desorbed, and these molecules could also be produced. The amount of desorbed gas due to a pressure drop from P_1 to P_2 is given as the difference between the amounts of gas sorbed at these pore pressure values as calculated using Langmuir's model in equation (2).

However, the production of the absorbed fluid in micropores is quite challenging, since these are the dissolved fluid molecules in the solid kerogen, and are under the strongest influence of the pore walls. The density of the fluid dissolved in the kerogen is so high that it could be comparable to that of the same fluid in the liquid phase. Diaz-Campos (2010) previously showed that carbon dioxide residing in nanopores could have a high density (comparable to the liquid phase), especially the molecules that are by the pore walls. (See **Figure 1.1.**).

These results indicate that the sorption mechanisms could lead the naturally-occurring (gaseous) fluids such as methane and CO_2 into liquid-like or capillary-condensed phases under the reservoir conditions depending on the reservoir pressure, temperature and organic nanopore size.

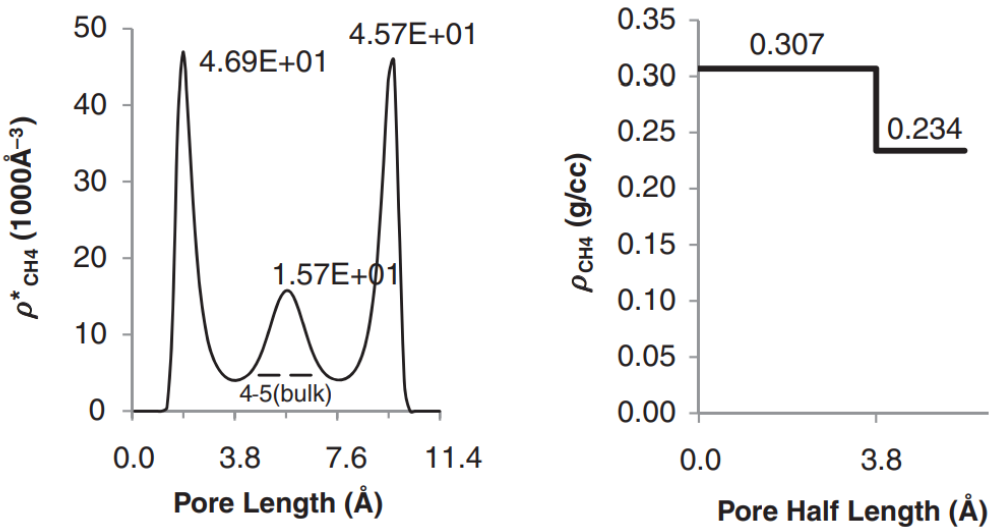

Figure 1.1. Density Profile of Methane in 1.14 nm Organic Slit-pore as a Function of Distance from the Pore Wall to the Center of the Pore at 3043 psi Pore Pressure and 176 F (80 C) Temperature. Reprinted from Diaz-Campos, 2010.

Chen et al. (2013) considered the presence of liquid hydrocarbons in the small pores where capillary condensation occurred. Adopting Kelvin's equation, the critical size r_{cp} – the pore size below which capillary condensation occurs – for pure fluids is given as:

$$r_{cp} = -\frac{2\lambda V_L \cos\theta}{RT \ln\left(\frac{p_v}{p_d}\right)} \quad \text{..... (11)}$$

They suggested that pores smaller than r_{cp} are completely filled with liquid hydrocarbons. For pores larger than r_{cp}, they adopted the Langmuir model to determine the adsorbed gas amount, and consequently, the hydrocarbon-in-place.

1.3.2. Multi-Component System

In multi-component systems, selective adsorption takes place by the nanopore walls. The selective adsorption is based on the level of interaction between the molecules of each component in the fluid mixture with the wall atoms – the higher the level of interaction of a component's molecules with the wall, the more those molecules are adsorbed at the expense of molecules with a lower level of interaction with the wall.

In general, heavier hydrocarbons with larger molecular structure are adsorbed at the expense of the lighter ones. For instance, Al Ismail and Horne (2014) reported that for a methane/*n*-butane mixture in a variety of pore sizes, n-butane gets preferential adsorption over methane, even at low pressures.

Bui and Akkutlu (2017), Baek and Akkutlu (2019b, 2019c) showed that the adsorption layer composition by the wall is rich in the heaviest molecules of the mixture, while the center of the pore is rich in the lightest molecules of the mixture. The adsorbate for a multi-component system has a higher density than that in a pure methane system. This is because the adsorbate is a heavy hydrocarbon mixture. The center of the pore is usually composed of a lighter free gas mixture.

Baek and Akkutlu (2019b, 2019c) also explained that with decreasing pore size, less of the lighter hydrocarbons are contained in the pore; leading to an increase in the concentration of the heavy components, and subsequently, an increase in the average

density of the fluid mix in the pore. With increasing pore size, on the other hand, there is an increase in the concentration of the lighter components of the mixture at the center of the pores. Baek and Akkutlu (2019c) termed this phenomenon ‘nanoconfinement effect’. (See **Figure 1.2.**).

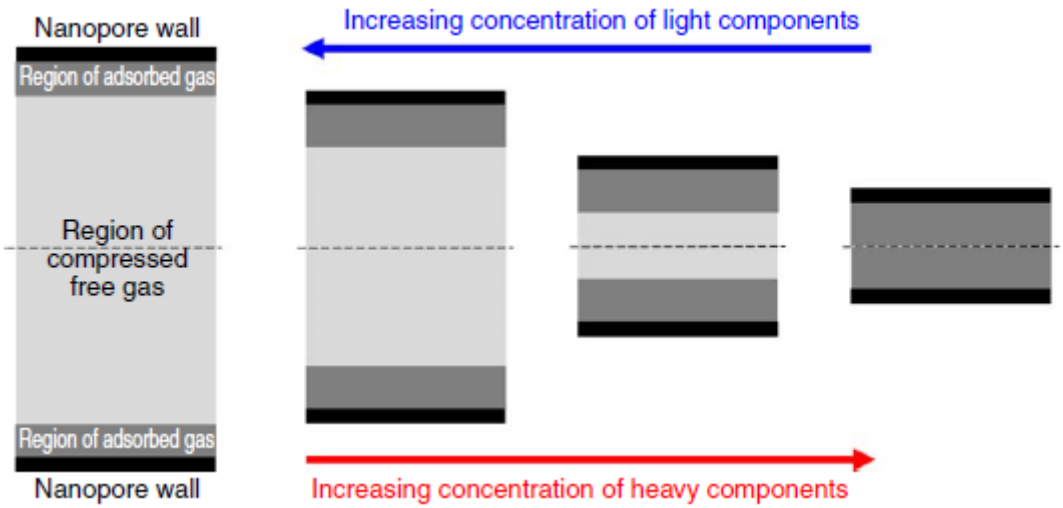

Figure 1.2. Nanoconfinement effect. Reprinted from Baek and Akkutlu, 2019c.

Further studies by Didar and Akkutlu (2015) show the influence of nanoconfinement on the fluid mixture. They reported that the nanoconfined fluid has different thermodynamic behavior (including P-T diagram) than fluid in the bulk phase. They stated that, for multi-component fluids, the phase diagrams tend to shift drastically when there is an increase in the concentration of light components. This is corroborated by the work of Pitakbunkate et al. (2016).

Baek and Akkutlu (2019c) proposed that the compositional shift in fluid mix due to nanoconfinement can be captured using the so-called produced fluid composition redistribution calculations. They proposed a new volumetric equation which considers the nanoconfinement effect explicitly as part of a modified formation volume factor

description. They also discussed the development of capillary condensation of fluid mixtures in the nanopores. **Figure 1.3.** shows their observation of capillary condensation on the density-pressure phase diagram of the fluid mixture in the presence of nanoconfinement effect. Clearly, the fluid mixtures residing in nanopores (each pore with its own redistributed hydrocarbon mixture composition) is experiencing capillary condensation, even though there are no indications of capillary condensation of the bulk mixture of the same fluid (yellow line).

Another important aspect of the figure is the vaporization of the capillary condensed hydrocarbon mixture taking place at an observed 'bubble point' pressure, which seems to be dependent on the nanopore size. For instance, the vaporization of the fluid mix in the 6nm pore develops around 500 psi pore pressure, and in 4 nm pore, it is around 300 psi. The vaporization of the fluid seemingly becomes significantly more difficult as the pore size shrinks – the fluid in 2nm pore requires for the pore pressure to be dropped to around 50 psi. In these scenarios, fluid vaporization will require pumping off the wells, to the point of applying vacuum in certain cases, in order for operators to drop the pore pressures to low enough values for the capillary condensed fluids to reach vaporization. From a practical point of view, the reduction in vaporization pressure indicates that recovery from the organic nanopores will be challenging, if not practically impossible.

For multi-component fluids, Chen et al. (2013) adopted the following critical capillary radius for the onset of capillary condensation:

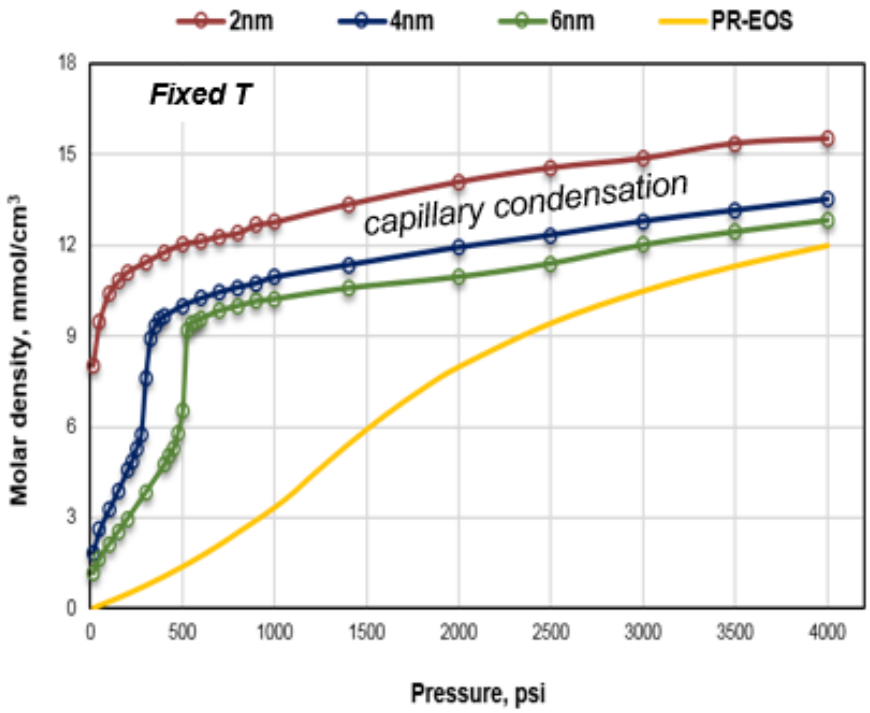

Figure 1.3. Density-pressure phase diagram of the fluid mixture in the presence of nanoconfinement effect. Adapted from Baek and Akkutlu, 2019b.

$$r_{cp} = \frac{2\lambda \cos\theta}{p_d\left[\frac{V_{vl}(p_d,y)}{V_l(p_d,x)} Z_{av}(y_v) \ln X - X + 1\right]} \quad \text{..... (12)}$$

However, although this equation could possibly give a rough estimate for the onset of capillary condensation, it does not consider the composition variability in the fluid mixtures residing in nanopores.

1.4. Normalized Pore Composition

For multi-component fluids, Bui and Akkutlu (2017) and later Baek and Akkutlu (2019a, 2019c) expressed the compositional differences between the fluids in the bulk phase and the fluid in the nanopores using normalized pore composition plots. The normalized pore composition of a single component in the fluid is the ratio of that

component's composition in the nanopore to its composition in the bulk fluid. Hence, a unity normalized composition value indicates that the component's composition in the nanopore fluid is the same as its composition in the produced fluid.

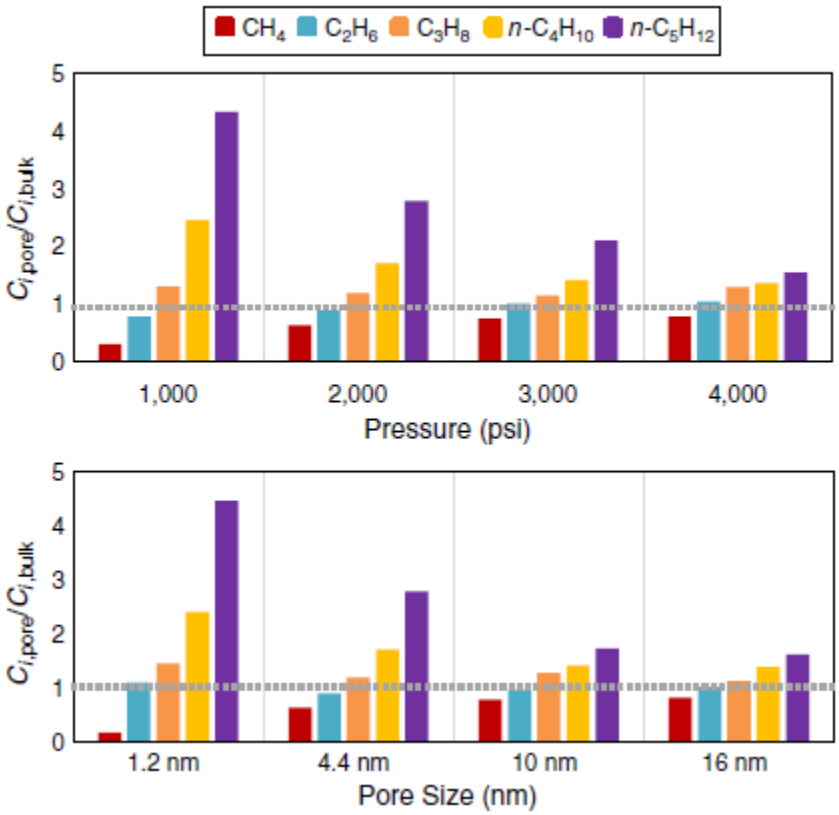

Figure 1.4. Normalized Pore Composition of a Quinary Mixture in a 4.4 nm Pore (top), and at 2000 psi (bottom). Reprinted from Baek and Akkutlu, 2019c.

Baek and Akkutlu (2019c) discussed that the compositional difference (normalized pore composition) is dependent on pressure, pore size and temperature. They showed that in relation to the bulk fluid composition (unity normalized pore composition), the heavy components in the fluid in a single nanopore increased with decrease in pressure (due to pressure depletion and production), while the composition of the light hydrocarbons reduced. For a constant pressure scenario, for example at the initial reservoir pressure, the

fluids in the smaller pores contained more of the heavier components than the lighter ones. (See **Figure 1.4.**). This observation corroborates the nanoconfinement effect.

1.5. Thermodynamic Hydrocarbon Recovery Computations

Baek and Akkutlu (2019a) stated that hydrocarbons can be produced from the organic-rich shale reservoirs via two recovery mechanisms: fluid expansion, and molecular desorption. Based on their molecular simulations, they reported that the free gas in the pores above 40 nm in size are produced mainly due to the expansion of the fluid in the pore. When a finite volume of fluid leaves the pore and is produced, the void created by the production is filled up by the expansion of the fluid left behind in the pore. This accounts for up to 50% of the hydrocarbons in-place. Below the threshold pore size, however, more of the fluid molecules are held in sorbed states, and these fluid molecules have to be first desorbed (or released by the pore walls) in order to be recovered. Unfortunately, desorption is not as effective a recovery mechanism as fluid expansion. Consequently, a sharp drop is observed in the production from the 40 to 10 nm pores – to the levels of recovery typically less than 20%, as recovery is forced from truly small organic nanopores. (See **Figure 1.5.**).

Li et al. (2016) adopted the extended Langmuir model to determine the composition of the desorbed gas. Considering that the different components will have different desorption capacities, then the amount of gas desorbed for component i in the mixture at a given pressure change (Δp) can be expressed as:

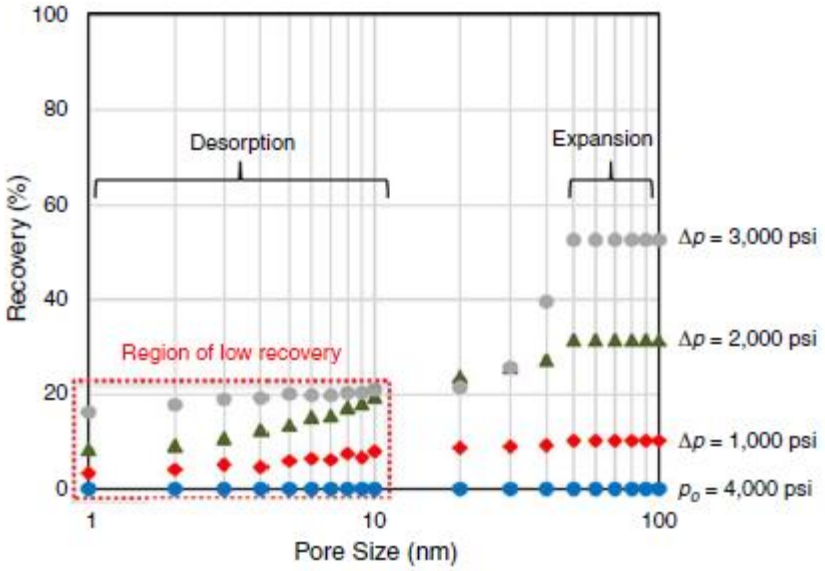

Figure 1.5. Fluid Recovery due to Desorption and Fluid Expansion Mechanisms Reprinted from Baek and Akkutlu, 2019a.

$$\Delta G_{a,i}(p) = G_{a,i}(p+\Delta p) - G_{a,i}(p-\Delta p) \quad \text{..... (13)}$$

Adopting equation (7), equation (13) can be further expanded into:

$$\Delta G_{a,i}(p) = \frac{G_{sLi}y_i}{p_{Li}}\left[\frac{p+\Delta p}{1+\sum_{j=1}^{m} y_j \frac{p+\Delta p}{p_{Lj}}} - \frac{p-\Delta p}{1+\sum_{j=1}^{m} y_j \frac{p-\Delta p}{p_{Lj}}}\right] \quad \text{..... (14)}$$

Hence, the total desorbed gas volume can be expressed as:

$$\sum_i \Delta G_{a,i}(p) = \sum_i \left[G_{a,i}(p+\Delta p) - G_{a,i}(p-\Delta p)\right] \quad \text{..... (15)}$$

The desorbed gas composition for a component i will be obtained by dividing equation (14) by (15).

1.6. Produced Fluid Composition Redistribution

The previous discussion indicates the possibility that the composition of the recovered hydrocarbons is different than the composition of the in-situ fluid. This is

further complicated by nanopore confinement effect, which causes the fluid composition to vary by pore size.

Bui and Akkutlu (2017) investigated the recovery of two quinary mixtures (containing CH_4, C_2H_6, *n*-C_3H_8, *n*-C_4H_{10} and *n*-C_5H_{12}) via molecular simulation, by simulating production of fluid molecules in nanopores to a nearby microfracture via a pressure drop in the system from 4000 psi to 1000 psi. They reported that from pores smaller than 2 nm, only 14% of the first quinary mixture was recovered, and 16% of the second mixture. They attributed the low recovery to the strong influence of the pore walls in trapping the fluids in an adsorbed state. Greater amounts of fluids were recovered from larger pores, due to the presence of more free gas. For instance, they reported that 22% of fluids were recovered from a 16 nm pore.

To compare the composition of the produced fluid with that of the in-situ fluid, Bui and Akkutlu (2017) defined a parameter called the confinement effect (CE); which is the ratio of the molar fraction of each component inside the pore with that bulk fluid outside the pore:

$$CE_i = \frac{molar\ fraction\ of\ i\ inside\ the\ pore}{molar\ fraction\ of\ i\ outside\ the\ pore} \quad \text{..... (16)}$$

The CE values for the components in the quinary mixtures show that the composition in and outside the pores are different for each of the components. CE is a function of both pore pressure and size; as pore size increases, the confining effect diminishes and tends to unity. Heavier components also tend to have higher CE values.

Baek and Akkutlu (2019c) further studied how the composition of the produced fluids measured in the field can be ‘redistributed’ into the nanopores in the reservoir. The

process of redistributing the produced fluid is essential in determining the density of the in-situ fluid, before using volumetric methods to determine the hydrocarbon in place. They identified a cutoff pore size ($d_{p,L}$), below which the density of the fluid in the pore is higher than that in the bulk phase. For a pore size (d_p) which is less than $d_{p,L}$, the density of the fluid is given in relation to the density of CH_4 in that pore (ρ_{dp,CH_4}) and density of CH_4 in the bulk phase (ρ_{bulk,CH_4}) as:

$$\frac{\rho_{dp,mix}/\rho_{bulk,mix}}{\rho_{dp,CH_4}/\rho_{bulk,CH_4}} = a \times \ln d_p + b \quad (17)$$

where a and b are dimensionless coefficients given as a function of the density of the fluid in the bulk phase ($\rho_{bulk,mix}$):

$$a\left(\rho_{bulk,mix}\right) = -2.0072\rho_{bulk,mix}^2 + 2.0930\rho_{bulk,mix} - 0.4565 \quad (18)$$

$$b\left(\rho_{bulk,mix}\right) = 6.1421\rho_{bulk,mix}^2 - 6.6553\rho_{bulk,mix} + 2.4843 \quad (19)$$

Taking nanoconfinement effects into consideration, Baek and Akkutlu (2019c) estimated the gas in place to be:

$$G^*(p) = 32.0368\frac{\phi(1-s_w)}{\rho_b B_g^*} \quad (20)$$

where B_g^*, the formation volume factor (FVF) with nanoconfinement effects, is given as:

$$B_g^* = \frac{4.22092\times10^{-5}}{\upsilon\times\rho_{bulk,mol}+\sum_{d_{p1}}^{d_{pL}}\frac{V_{\%,d_p}}{100}\times\rho_{dp,mol}} \quad (21)$$

The molar density of the fluid in a nanopore of size d_p ($\rho_{dp,mol}$) is given as:

$$\rho_{dp,mol} = [c \times \ln\left(d_p\right) + d] \times \left(\frac{\rho_{dp,mol,CH_4}}{\rho_{bulk,mol,CH_4}}\right) \times \rho_{dp,mol} \quad (22)$$

where c and d are dimensionless coefficients given as a function of the molar density of the fluid in the bulk phase ($\rho_{bulk,mol}$):

$$c(\rho_{bulk,mol}) = -26159.41\rho_{bulk,mol}^2 + 599.0111\rho_{bulk,mol} - 3.3265 \quad \text{(23)}$$

$$d(\rho_{bulk,mol}) = 92405.03\rho_{bulk,mol}^2 - 2121.03\rho_{bulk,mol} + 12.8323 \quad \text{(24)}$$

1.7. Purpose of Study

This study attempts to redistribute a produced 20+ component condensate fluid. This was achieved via an NVT simulation using LAMMPS. The methodology is similar to that employed by Baek and Akkutlu (2019c). Their study was limited to fluids with little or no liquid content. The purpose of this study is to investigate the behavior of liquid-rich condensate fluid in production, and potentially, the limitations of the equation of state (if any) proposed by Baek and Akkutlu (2019c). Emphasis will be placed the compositional variability of the condensate fluid with nanopore size, its recovery mechanisms, and the existence of capillary condensation in the nanopores. Vaporization pressure as a function of pore size will also be investigated.

To reduce the computational complexity of the simulation, the 20+ components were broken into a smaller number of pseudo-components. The method employed is discussed in Chapter 3, and the results given in Chapter 4. The next chapter explains the theory supporting the computational method employed to investigate the nanoconfinement effect on the condensate fluid.

2. NUMERICAL SIMULATION

Although laws of nature can generally be expressed mathematically, most of them cannot be solved analytically. For instance, even though Newton's laws of motion are relatively simple, solving for the motion of many interacting bodies becomes impossible. With the advent of computers and numerical simulations, however, the solutions to these problems become achievable to a certain degree of accuracy. (Frenkel and Smit, 2002).

Before numerical simulations were employed in solving for these problems, theories were usually developed to give an approximate estimation of the parameter of interest. With numerical simulations, the results derived are comparable to those of experimental system, provided that the parameters for the simulations are accurate. (Frenkel and Smit, 2002). In general, numerical simulations are employed when the experiments are too dangerous to be carried out, or are infeasible.

In this work, numerical simulation is employed to investigate and make necessary measurements from the interaction between molecules of the fluid of interest. This is termed molecular dynamics.

2.1. Molecular Dynamics Simulation

Molecular dynamics is based on the results of the scientific works of Euler, Hamilton, Lagrange and Newton. (Rapaport, 2004). The technique is used in determining the equilibrium state and transport properties of a many-body system. Essentially, the bodies in the system are assumed to obey the law of classical mechanics, especially

Newton's second law of motion. (Frenkel and Smit, 2002). This assumption is viable where quantum effects can be neglected. (Balbuena and Seminario, 1999).

In molecular dynamics, the bodies in the system are the molecules of the investigated substance, which could either be solid, liquid or gas. The molecules are assumed to be spherical particles that interact with one another. The interaction could be in either of two forms: a resistance to compression (repulsion), or an attraction. These interactions are based on a potential function. (Rapaport, 2004).

The molecules are represented as rigid spheres. For example, a methane molecule with its tetrahedral structure can be represented as a single sphere, whereas a pentane molecule can be represented by five spheres, each representing a methyl group. This representation of hydrocarbon molecules is known as the United Atom approach. (Martin and Siepmann, 1998; Shah, et al., 2017). During the simulation, the individual trajectories of the spheres are modeled and monitored as these spherical bodies interact with each other and with the atoms that make up the pore walls. When the system reaches a state of equilibrium, the thermodynamic properties of interest (such total energy of the system, viscosity or self-diffusivity of the fluid molecules, or the average pore pressure) are then measured. As with real experiments, the measurements could be subjected to statistical noise; hence, the need to average the measurements. (Frenkel and Smit, 2002).

Before these thermodynamic properties can be measured, they need to be expressed in terms of the overall momentum of the molecules in the system. For instance, the operational definition of the temperature of the system is defined in terms of the average kinetic energy per degree of freedom:

$$\frac{1}{2}mv_{\alpha}^{2} = \frac{1}{2}k_{B}T \text{..... (25)}$$

In practice, however, the temperature at an instance (t) is obtained by computing the total kinetic energy of the system at that instance, and dividing by the number of the degrees of freedom (N_f):

$$T(t) = \sum_{i=1}^{N} \frac{m_i v_i^2(t)}{k_B N_f} \text{..... (26)}$$

where N_f, in a 3-dimensional space, is given as:

$$N_f = 3N - 3 \text{..... (27)}$$

where N is the number of molecules in the system.

Molecular dynamics involves a three-step process: modeling the individual molecules (initialization), simulating the movements of the molecules in the system until a state of equilibrium is reached (equilibration), and production – analyzing the simulation data for the measurements of the properties of interest. (Haile, 1992).

2.2. Initialization

Initialization is the assignment of initial positions and velocities to the molecules, and the configuration of the boundary conditions. In this study, the initialization process involved defining the boundaries of the computational box, building the pore walls, determining the number of fluid molecules required for the compositional mixture at the pressure of interest, and assigning the fluid molecules to their initial positions. In setting these initial configurations, consideration has to be made for the properties of interest of the molecules/system. (Sharma, 2019). Since the purpose of molecular dynamics is to

sample a region in an entire system, an implied corollary is that the equilibrium state of that system is independent of the initial state of the system. (Rapaport, 2004).

2.2.1. Initial Positions

Since the equilibrium state of the system is independent of the initial conditions, it is possible to assign random coordinates to the spherical molecules. This is, however, not advisable, as it could lead to an overlap of the molecules and low packing fractions. (Sharma, 2019). Hence, it is recommended that the molecules of a solid to be simulated be configured in the solid's crystal structure. For fluids, the molecules can be configured in a convenient crystal structure. (Frenkel and Smit, 2002). The crystal lattice structures are not subjected to overlaps and achieve a high packing fraction. (Sharma, 2019).

Preferably, the final (well-equilibrated) positions of the molecules from a previous simulation should be used as the configuration for a new simulation. When this is not available, the molecules can be arranged in a crystal lattice with significant packing fractions. (Frenkel and Smit, 2002).

2.2.2. Initial Velocities

As with the positions of the molecules, the velocity for the individual molecules could be carried over from a previous simulation. When this previous configuration is unavailable, the initial velocity is defined as a function of the temperature of the system – in accordance with Maxwellian distribution. (Sharma, 2019):

$$f(v_i) = \left(\frac{m}{2\pi k_B T}\right)^{\frac{3}{2}} \exp\left\{-\frac{m}{2k_B T}\left(v_{ix}^2 + v_{iy}^2 + v_{iz}^2\right)\right\} \quad (28)$$

where $f(v_i)$ is a probability density Maxwellian distribution function for the velocity of molecule i. The velocities of the molecules are then translated, such that the total

momentum of the system is zero. At the thermal equilibrium of the system, equations (25) and (26) are expected to hold. (Frenkel and Smit, 2002).

2.2.3. Boundary Conditions

This involves defining the coordinates of the simulation box containing the simulated molecules, and the behavior of the molecules at the defined boundaries. To help simulate and understand bulk fluid behavior (as opposed to wall-fluid interactions), it is necessary to adopt periodic boundary conditions – such that the fluid molecules that exit at a boundary re-enter the system at the opposite boundary.

This is achieved by simulating a number of molecules in a primary cell of known volume, which is only a representative of the bulk material, such that the bulk material is composed of the primary cell surrounded by exact replicas of itself. These replicas are termed the image cells. Essentially, the primary cell is periodically replicated in all directions to form a bulk (macroscopic) sample of the investigated substance. (Haile, 1992).

2.3. Equilibration

After initializing the system, by configuring the molecules in a crystal lattice with high packing fractions, the molecules follow a trajectory to reach a state of equilibrium – a region of space in the system that is most accessible to the molecules. (Haile, 1992). The equilibrium state is the state where the energy of the system is at a minimum, that is, all the forces on the molecules are balanced. (Mackay, et al. 1989).

Before and after the system equilibrates, the molecules follow trajectories based on the forces acting on them. Although the equilibrium state of the system is independent

of the initial configuration – that is, measurements at the final state are always reproducible, subject to statistical fluctuations – the trajectories leading to the final state may be different for different simulations/machines. This is due to the exponential sensitivity of the trajectories to even the most minute perturbations. (Rapaport, 2004).

The trajectory of each molecule is determined by evaluating the position of the molecules at a timestep. One of the more common methods of evaluating the trajectories is the velocity Verlet method. In this method, after the initial configuration is specified, the forces acting on all molecules are calculated. Using the calculated force in Newton's second law of motion, the positions and velocities of the molecules are evaluated for the next time step. The forces at the next time step are evaluated, and the process is repeated.

2.3.1. Force Fields

A force field refers to the mathematical expression describing the potential energy of a system of molecules and/or atoms. It could also be used to analytically reproduce the geometry of the molecules in the system. The parameters used to define force fields could either be derived experimentally, or via quantum mechanical calculations. When the parameters define the force field between individual atoms in the system, it is termed all-atom force field. If, on the other hand, the parameters define the force field between methyl and methylene groups (in hydrocarbons), it is termed a united-atom force field. (Sharma, 2019). Force fields are also useful for showing the relationship between the energy of a system and the coordinates of the associated molecules. (Gonzalez, 2011).

Force fields account for molecules/particles bonded together by covalent bonds, and the interaction between nonbonded molecules/particles under the influence of

electrostatic and van der Waals forces. Essentially, force fields can be expressed mathematically as:

$$E_{total} = E_{bonded} + E_{nonbonded} \quad (29)$$

2.3.1.1. Bonded Force Field

The first term on the RHS of equation (29) models the covalent contributions, that usually do not allow for bond breaking. This includes the covalent interaction between 2 molecules (bonds), 3 molecules (angles), and 4 molecules (dihedrals and impropers). Hence, E_{bonded} in equation (29) can be expressed as:

$$E_{bonded} = E_{bond} + E_{angle} + E_{dihedral} \quad (30)$$

The individual terms on the RHS of equation (30) are modeled as harmonic oscillators (Sharma, 2019):

$$E_{bonded} = \sum_{bonds} \frac{1}{2} k_{bonds}(l - l_0)^2 + \sum_{angles} \frac{1}{2} k_{angles}(\theta - \theta_0)^2 + \sum_{dihedrals} \frac{1}{2} k_{dihedrals}(1 + \cos(n\omega - \gamma)) \quad (31)$$

2.3.1.2. Nonbonded Force Field

The second term on the RHS of equation (29) accounts for the intermolecular electrostatic and van der Waals interactions:

$$E_{nonbonded} = E_{electrostatic} + E_{vanderWaals} \quad (32)$$

The electrostatic and van der Waals forces are typically modeled via Coulomb's Law and Lennard-Jones potential respectively.

Originally proposed for liquid Argon, Lennard-Jones potential models the potential energy between two neutral molecules i and j, at a distance r_{ij} from each other as:

$$E_{vanderWaals} = 4\epsilon\left[\left(\frac{\sigma}{r_{ij}}\right)^{12} - \left(\frac{\sigma}{r_{ij}}\right)^{6}\right] \quad \text{..... (33)}$$

Equation (33) models both the short-range repulsion (the positive first term on the RHS), and the longer-range attraction (the negative second term on the RHS) potentials of the interaction between molecules i and j. When r_{ij} is greater than or equal to a cutoff distance r_c, the potential energy as modeled by equation (33) is zero. As the molecules draw closer, such that r_{ij} is less than r_c, the potential energy decreases (attraction) until it reaches a minimum 'well depth' energy value ϵ. As the molecules draw closer still, the energy increases (repulsion), until it reaches an energy value 0, at a distance σ. Further reduction of r_{ij} increases the repulsive energy very steeply. (See **Figure 2.1.**).

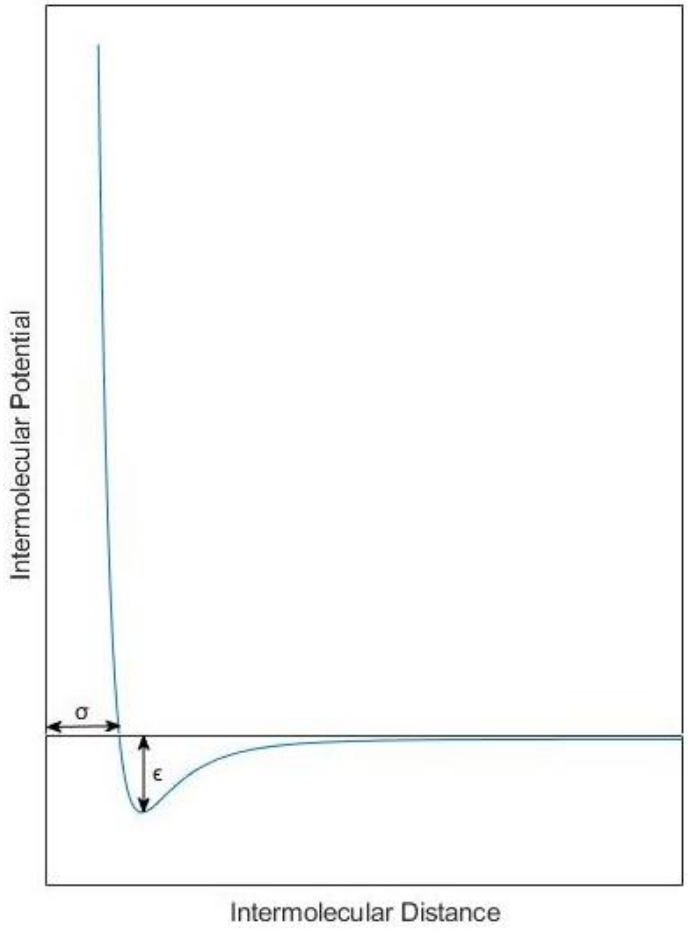

Figure 2.1. A Typical Lennard-Jones Potential Function

The electrostatic force between 2 charged nonbonded molecules i and j, at a distance r_{ij} from each other, with charges q_i and q_j respectively is modeled by Coulomb's law as:

$$E_{electrostatic} = \left[\frac{1}{4\pi\epsilon_0}\right]\frac{q_i q_j}{r_{ij}} \quad \text{..... (34)}$$

2.3.2. Neighbor Lists

For a molecule i in a system of N molecules, the energy or force calculations have to be evaluated for a total of $N-1$ pairs. Hence, the total number of pair interactions to

be accounted for is $N(N-1)/2$. This method of evaluating the pair interactions, for all available pairs in the system is called the 'all-pairs' method (Rapaport, 2004). The all-pairs method is time-consuming and computationally expensive.

A more efficient method is the neighbor lists method, where for every molecule i, only the interactions with neighboring molecules in a radius r_n around i are evaluated. r_n is evaluated as:

$$r_n = r_c + \Delta r \quad (35)$$

where Δr is an arbitrary small distance called skin, typically 0.3σ long. (Haile, 1992).

The efficiency of the neighbor lists method stems from the capability of using the same neighbor list over a number of timesteps. The list only has to be updated when the maximum displacement of the molecules in the list due to the forces exerted exceeds Δr. (Frenkel and Smit, 2002).

2.4. Production

Maximum entropy of the system is an indication that the system has attained a state of equilibrium. As entropy cannot be evaluated directly, a constant total energy of the system, and fluctuations of thermodynamic properties (temperature, internal energy and pressure) about stable average values, are good indications of equilibrium. (Haile, 1992).

Production runs are run after the system attains a state of equilibrium. The runs are made long enough to reduce the statistical uncertainties in the measurements of properties of interest. (Haile, 1992). In molecular dynamics, the runs could be in either of three ensembles: microcanonical ensemble (constant number of molecules N, constant volume

V, and constant energy E), canonical ensemble (constant number of molecules N, constant volume V, and constant temperature T), or isothermal-isobaric (constant number of molecules N, constant pressure P, and constant temperature T). The type of ensemble employed in the production run depends on the constraints that has to be applied to the system, to get the required measurements.

3. METHODOLOGY

This chapter focuses on the fluid samples and the adopted model for the simulation study. All the thermodynamic properties were computed using the Peng-Robinson Equation of State (Peng and Robinson, 1976) with Peneloux volume correction. (Peneloux et al., 1982).

3.1. Produced Fluid Sample

The investigated fluid sample is a 20+ component condensate fluid. The PVT laboratory analysis of the fluid had been completed previously. Using the full composition of the fluid, a fluid model was developed via the Peng-Robinson EoS, using the PVTSim software. The full-composition model compared favorably with the laboratory results and the critical quantities such as the dew point pressure (of the bulk fluid) and liquid volume collected. However, the full-composition model was too complex for the investigation. To ease the computational complexity of the molecular simulation, the fluid was first characterized into 5 pseudo-components. The pseudo-components and their properties are shown in **Table 3.1.**

The thermodynamic properties of the characterized fluid compared favorably with those of the 20+ component fluid across a wide range of pressure values – the density values had a maximum error of 0.96%, the Z-factor a maximum error of 0.74% and the gas viscosity had a maximum error of 5.65%.

Table 3.1. Produced Fluid Characterization

Pseudo-Component	Composition (%)	Critical Temperature (°F)	Critical Pressure (psia)	Acentric Factor
N_2+C_1	71.106	-117.557	665.7	0.0083
CO_2+C_2+C_3	17.923	137.025	694.6	0.1283
iC_4 – C_6	5.795	348.952	506.1	0.2229
C_7 – C_9	3.044	540.051	429.3	0.5009
C_{10+}	2.132	732.960	282.5	0.7409

The phase diagram for the characterized fluid mixture is shown in **Figure 3.1.** The temperature of interest, that is, the reservoir temperature is shown as the vertical dashed line in the figure at 107°F. The critical point of the fluid is at a temperature of 64.09°F and pressure 3195.9 psia. Since the initial reservoir pressure is approximately 8,000 psia, the fluid exists as a condensate gas at initial reservoir pressure. The dew point pressure (p_d) of this bulk fluid at reservoir temperature is about 3472.3 psia.

The fluid contained in the bulk phase in the reservoir has the same composition as the produced fluid. This is made up of all fluids in pores sizes greater than the cutoff pore size ($d_{p,L}$).

3.2. Produced Fluid Model

A simple concept was adopted to model the lumped produced fluid components in **Table 3.1.** A single hydrocarbon component from each pseudo-component was selected

to represent that pseudo-component. The selection was done such that the thermodynamic properties of the resulting fluid were comparable to that of the original 20+ component fluid. The selected hydrocarbon components are shown in **Table 3.2.**

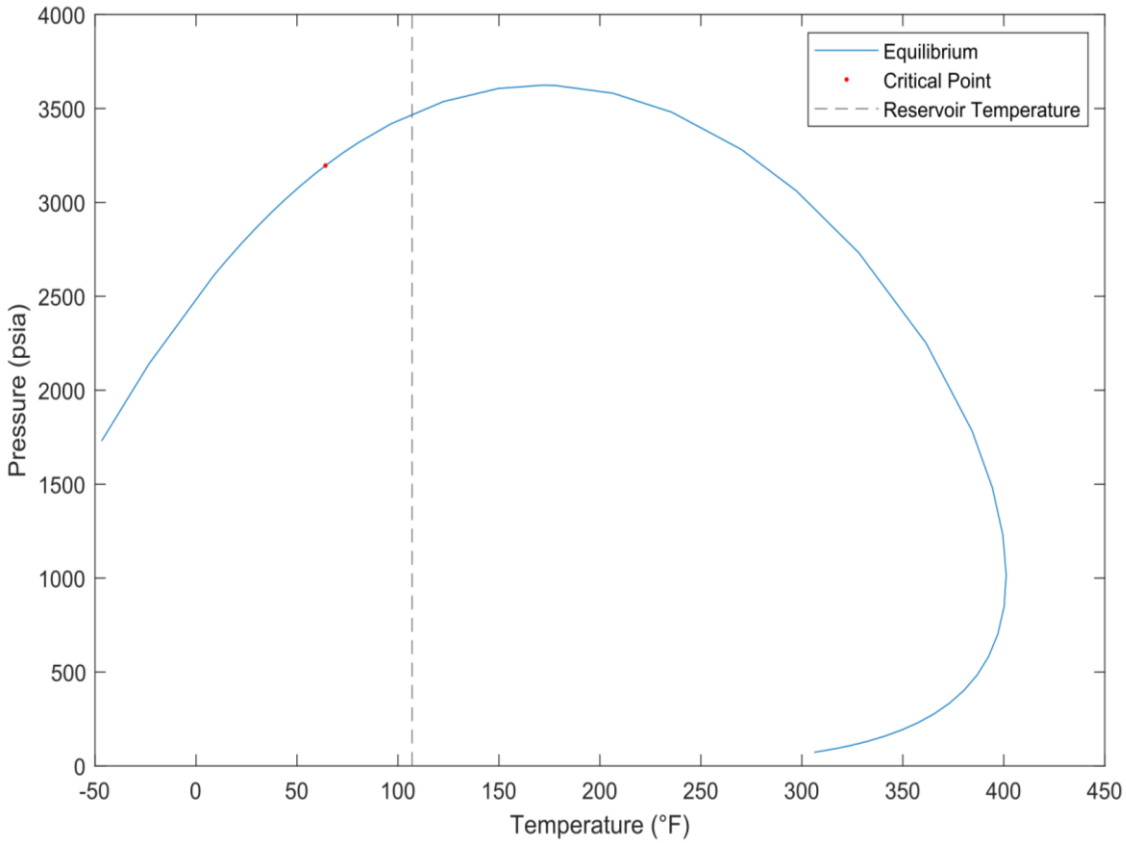

Figure 3.1. Pressure/Temperature Phase Diagram of the Fluid Mixture

Figure 3.2. shows the phase diagram of the model, and how it compares to the phase diagram of 5-pseudo-component fluid model given in **Figure 3.1.** Clearly, the model also exists as a condensate gas in the bulk phase at the reservoir temperature. The critical point of the model is at a temperature of 74.22°F at pressure 2932.4 psia. The dew point pressure at reservoir temperature is approximately 3126.4 psia.

Table 3.2. Produced Fluid Model

Hydrocarbon Component	Composition (%)
C1	71.107
C2	17.922
*n*C5	5.791
C7	3.040
C13	2.140

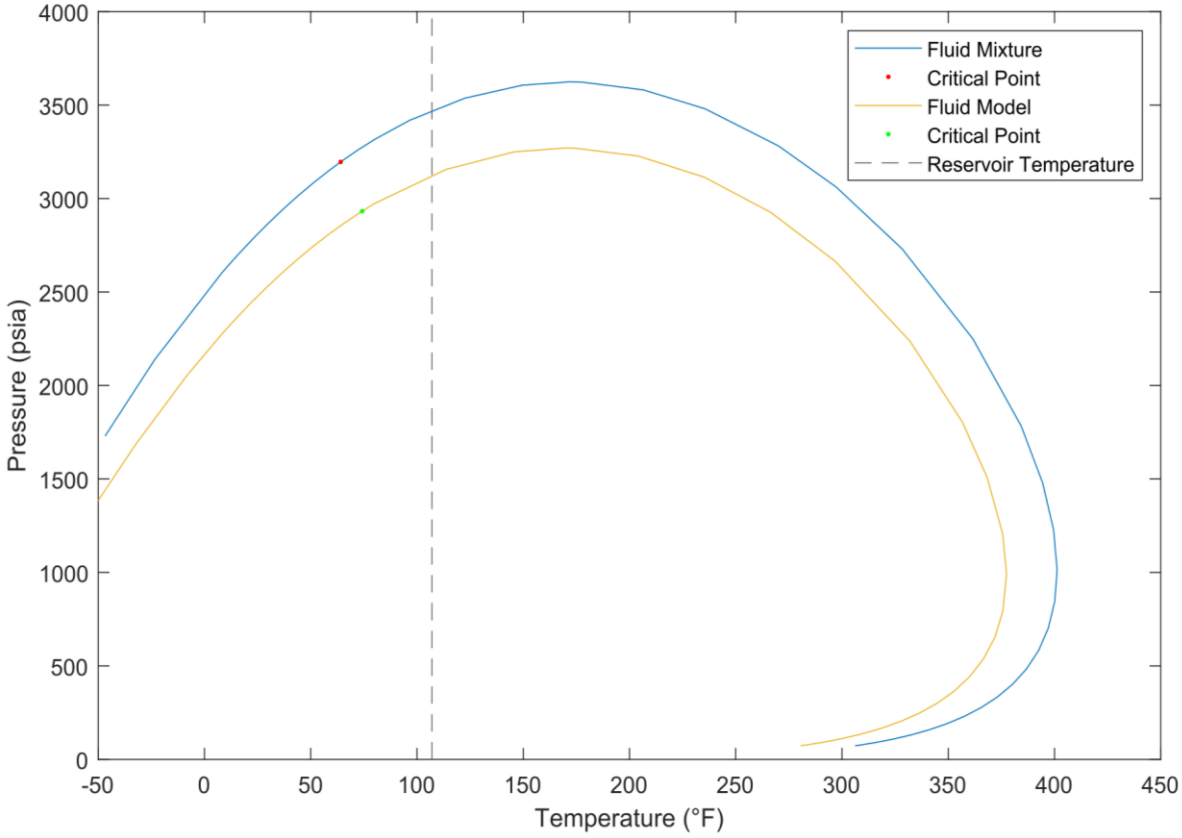

Figure 3.2. Pressure/Temperature Phase Diagram of the Fluid Mixture and Fluid Model

3.2.1. Produced Fluid Model Validation

To validate the 5-component produced fluid model, the bulk density and Z-factor of the fluid were compared to that of the original 20+ component hydrocarbon mixture across a range of pressures at 107°F. **Figure 3.3.** shows that both fluids have comparable thermodynamic properties. The error in the bulk density was highest at the lower pressures (4.81% at about 1000 psia), while the errors in the Z-factor were less than 3%.

3.2.2. Molecular Interactions

The interactions between the molecules were modeled using the transferable potential for phase equilibria (TraPPE) force field. The molecules were modeled using the United Atom force field approach, which improves computational efficiency (without sacrificing too much accuracy) by using single interaction sites (pseudo-atoms) to model a carbon atom with all of its bonded hydrogen atoms. (Martin and Siepmann, 1998; Shah, et al., 2017).

The nonbonded interactions were modeled via a sum of the Lennard-Jones potential and the Coulombic forces, i.e., a sum of equations (33) and (34):

$$E_{NB} = 4\epsilon\left[\left(\frac{\sigma}{r_{ij}}\right)^{12} - \left(\frac{\sigma}{r_{ij}}\right)^{6}\right] + \frac{q_i q_j}{4\pi\epsilon_0 r_{ij}} \quad (36)$$

For the Lennard-Jones interactions between 2 unlike pseudo-atoms, the standard Lorentz-Bethelot mixing rules were applied:

$$\sigma = \frac{1}{2}(\sigma_{ii} + \sigma_{jj}) \quad (37)$$

$$\epsilon = \sqrt{\epsilon_{ii}\epsilon_{jj}} \quad (38)$$

The spherical cut-off distance (r_c) was set as 14 Å.

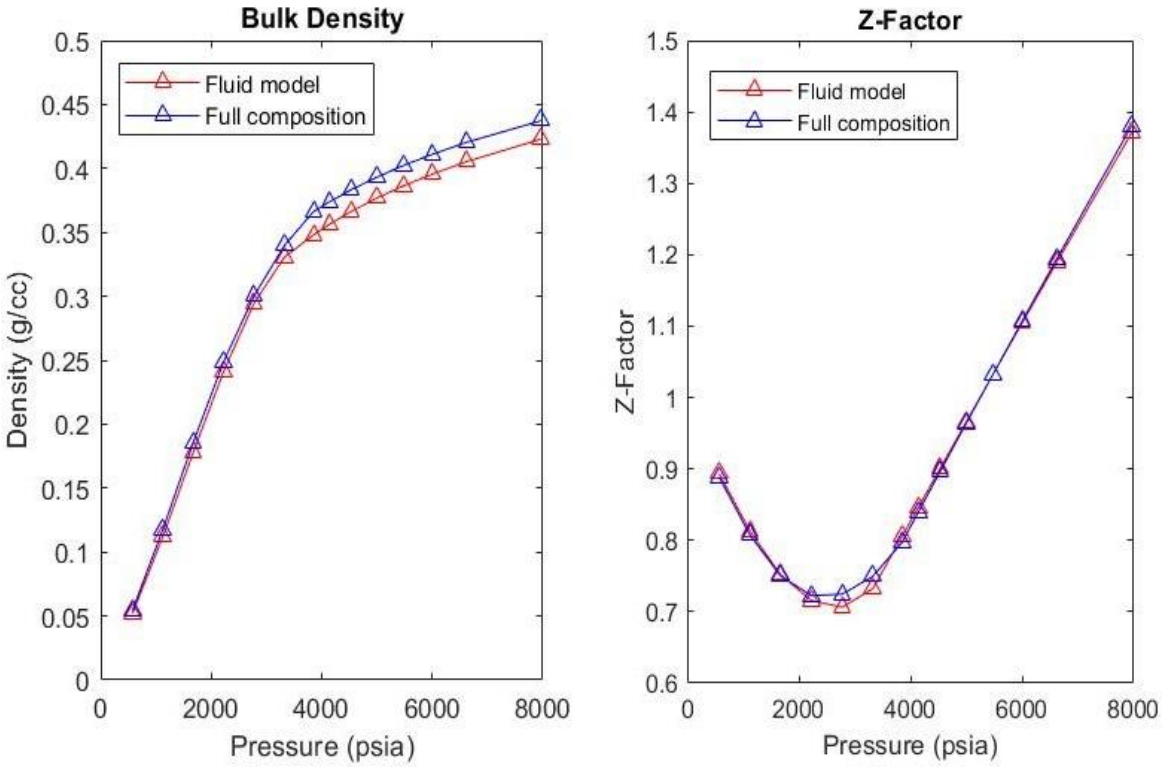

Figure 3.3. Produced Fluid Model Validation

The bonded interactions were modeled using equation (31). For the interaction between two molecules (bonds), TraPPE uses fixed bond lengths (l_0). The third term in equation (31) – which models the dihedrals – can, for one dihedral, be further simplified into:

$$E_{dihedrals} = \frac{1}{2}k_1(1+\cos(\phi)) + \frac{1}{2}k_2(1-\cos(2\phi)) + \frac{1}{2}k_3(1+\cos(3\phi)) + \frac{1}{2}k_4(1-\cos(4\phi)) \quad (39)$$

Table 3.3. summarizes the nonbonded interaction parameters of the pseudo-atoms, while **Table 3.4.**, **3.5.**, and **3.6.** show the bonded interaction parameters for bonds, angles and dihedrals respectively.

Table 3.3. Nonbonded Interaction Parameters of the Pseudo-Atoms

Pseudo-atom	ϵ/k_B **(K)**	σ **(Å)**	q **(e)**
CH_4	148	3.74	0.00
CH_3	98	3.75	0.00
CH_2	46	3.95	0.00
C	28	3.40	0.00

Table 3.4. Bonded Interaction Parameters of Bonds

Bond	l_0 **(Å)**
CH_x–CH_y or CH_y–CH_x	1.54

Table 3.5. Bonded Interaction Parameters of Angles

Angle	θ_0 **(°)**	k_{angle}/k_B **(K/rad^2)**
CH_x–(CH_2)–CH_y	114	62500

Table 3.6. Bonded Interaction Parameters of Dihedrals

Dihedral	k_1/k_B **(K)**	k_2/k_B **(K)**	k_3/k_B **(K)**	k_4/k_B **(K)**
CH_x–CH_2–CH_2–CH_y	0.00	355.03	–68.19	791.32

In defining the pairwise neighbor lists for the molecular interactions, a skin value (Δr) of 1.5 Å was used.

3.3. Bulk Fluid and Nanopore Model

In this study, the bulk phase was modeled as tanks, and the nanopore as carbon nanotubes. For each simulation, the computational box included two tanks connected by a nanotube. The two tanks were made of two walls (graphite sheets) each, 22 nm apart. Each graphite sheet was 60 nm wide and 50 nm high. The connecting carbon nanotube was 10 nm long, with varying diameters, depending on the nanopore size of interest. **Figure 3.4.** shows a 2D-view of the model.

3.4. Computational Methodology

For each simulation, the fluid molecules were initialized in the left and right tanks (i.e., the bulk phase). All molecules (fluid, tank walls, and nanotube wall) were contained in a simulation box with periodic x- and z- boundaries. The simulation box was approximately 60 nm wide, 55 nm long and 50 nm high, with its axis at the center of the nanopore.

To validate the molecular simulation approach, the bulk fluid was simulated using an NPT ensemble and compared with the Peng-Robinson EOS. **Figure 3.5.** shows that the bulk density measured from both models are comparable. The mean error between both models is 3.79%, the highest error being 7.43% at 3325 psia (around the dew point).

As the system equilibrated, some of the molecules located in the tanks migrated to the pore due to differences in chemical potential (see **Figure 3.6.**). At initialization, the tanks were charged with a large number of molecules, so that as some of the molecules

migrated to the nanopore, the composition of the fluid in the tanks remained effectively constant.

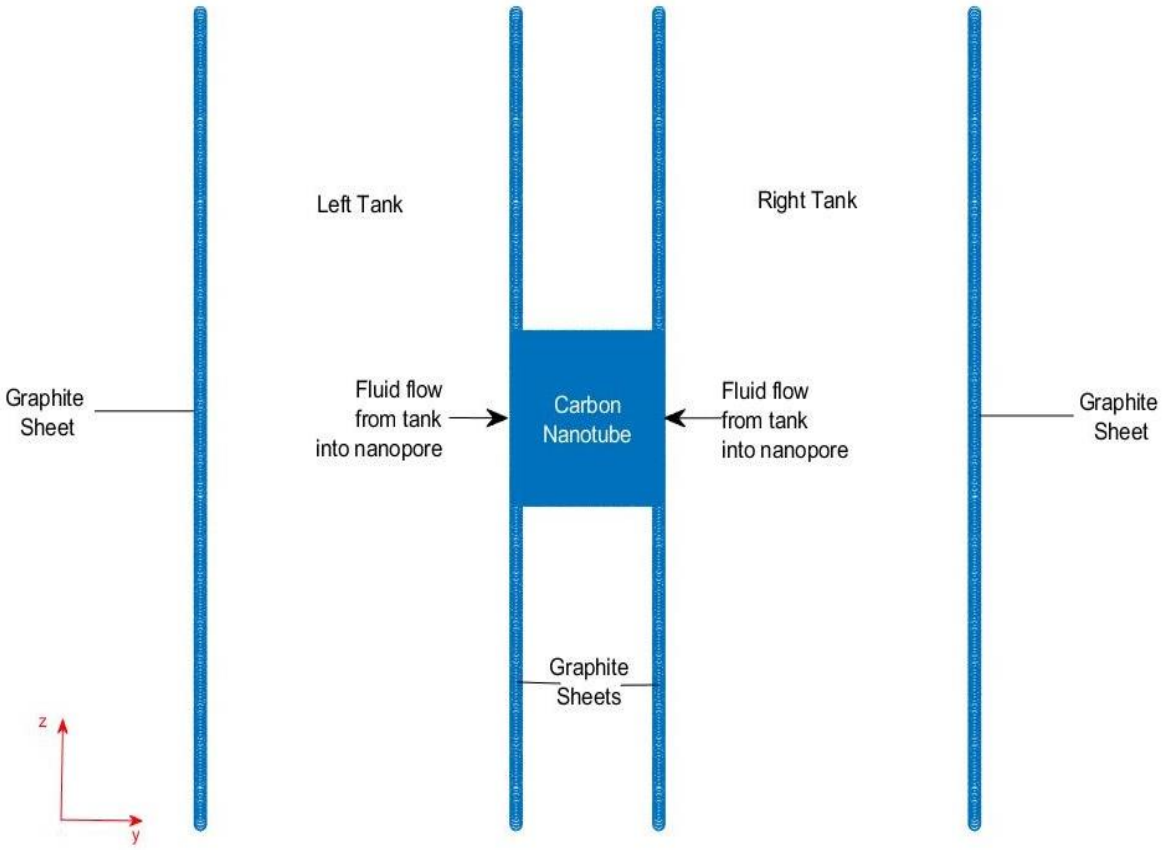

Figure 3.4. Y-Z Axes View of the Bulk Fluid and Nanopore Model

At equilibrium, the chemical potential of each species that make up the fluid becomes the same in the pore and in the tanks. Then, a number of simulations were run on the system using the NVT ensemble, to measure the pressure of the system, and the mass density of the fluids in the bulk phase and nanopore. The number of each fluid component in the nanopore was also counted, so that the composition of the fluid in the nanopores can be determined and compared with the composition of the fluid in the bulk phase.

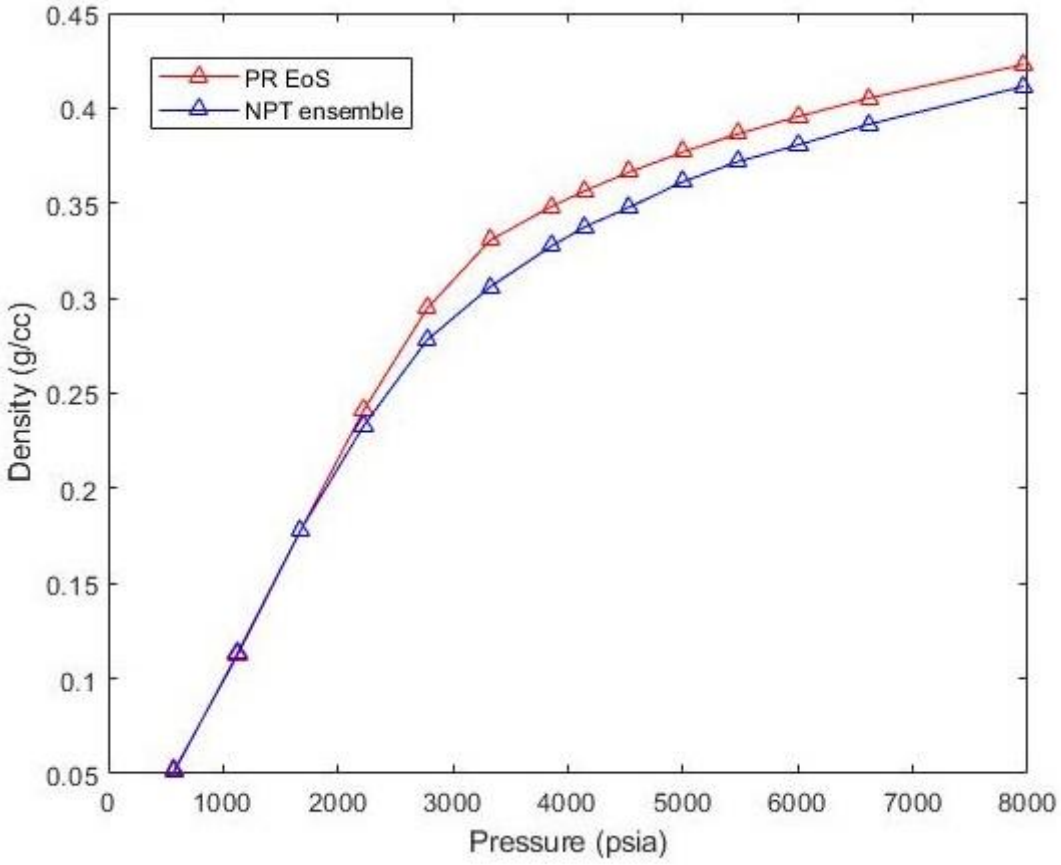

Figure 3.5. Computational Methodology Validation

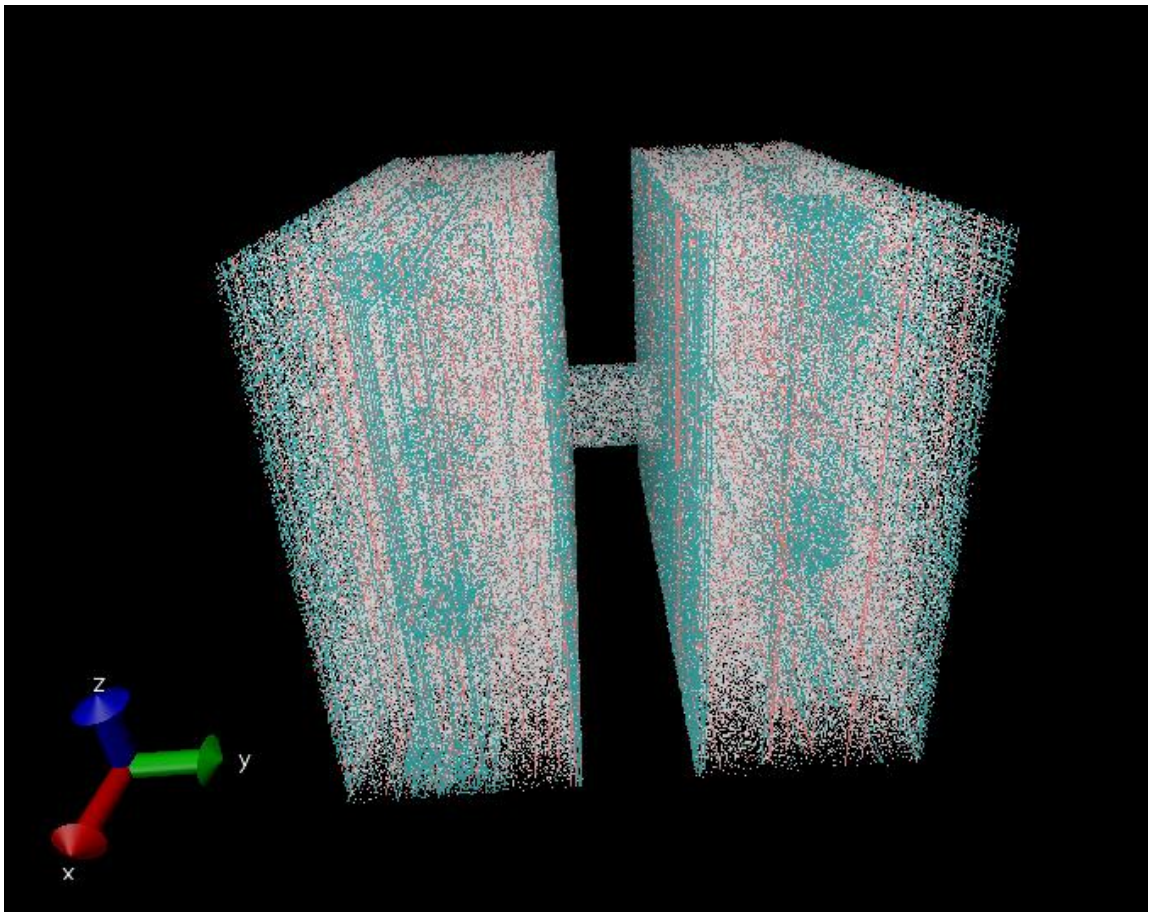

Figure 3.6. 3D Snapshot of the Fluid Molecules at Equilibrium.

4. RESULTS AND DISCUSSION

4.1. Redistribution of Produced Fluid Composition into Nanopores

As discussed previously, the thermodynamic properties of the fluids in the nanopores differ significantly from those of the fluids in the bulk phase due to nanoconfinement effect. In corroboration with the nanoconfinement effect, at constant pressure, the heavy hydrocarbons in the fluid mixture have a higher concentration in the small nanopores (at the expense of the lighter hydrocarbons), compared to their concentration in the bulk phase. Also, in the same nanopore size, the heavy hydrocarbons become even heavier at lower pressures. This phenomenon is discussed in Section 1 and shown in **Figure 1.4.**

Based on the sorption measurements and isotherm data available in literature, it is reasonable to assume that at high reservoir pressure (generally at pressure larger than 4000 psia and as high as 12000 psia), the organic pores would have adsorbed molecules enough to fully cover the pore walls surface; with the adsorbed molecules positioning themselves in a highly compacted fashion, minimizing the surrounding inter-particle space. Hence, in over-pressured reservoir systems with significantly high initial pressure, the organic nanopores should have reached their maximum sorption capacity. Then two questions arise: is the nanoconfinement effect influenced by this full coverage? Is the fluid in the pore expected to reflect this full coverage as a drastic change in compositional variability?

Firstly, reaching the maximum sorption capacity of the formation hints to the fact that the excessive amount of heavier components in the pore should leave the pore as part

of the effort for the fluid to maintain thermodynamic equilibrium. This should create an upper bound on the maximum concentration of the heavy component in the free fluid. Secondly, the full-coverage of the pore walls create a molecular blanket effect reducing the wall's influence on the free fluid molecules. In the latter case, the free fluid in nanopore have reduced effect of the nanoconfinement and behave as a bulk fluid.

These high-pressure effects are observed in this study. **Figure 4.1.** shows that at high pressure, there is no preferential storage of the heavy hydrocarbons in small nanopores at the expense of the lighter ones, or increased concentrations of light hydrocarbons with increasing nanopore size. Essentially, for this condensate fluid at 8,000 psia, although the heavy hydrocarbons (C_5 and C_7) in the nanopores had slightly more concentration than the lighter ones, all the components had normalized pore composition values close to unity (dashed line in the figure). This suggests that at high pressure the fluid in the nanopores is closest in composition to the bulk fluids located in the surrounding tanks.

A potential explanation for this observation is that when the source rock has become over-pressured during fluids generation, the structure, composition and properties of the adsorbed phase becomes established in the organic nanopores, and at some point, become insensitive to further increasing pressure. But further increasing pressure due to catagenesis continues to impact the fluid storage in the formation by forcing the lighter hydrocarbon molecules into the nanopores. Hence, during the fluid generation and over-pressure development, as the entire surface area of the nanopores is completely imbued with the heavy hydrocarbons in an adsorbed state, more of the lighter hydrocarbons are

charged into the central portion of the nanopores. This causes an increase in the composition of the lighter components, causing the overall fluid composition in the nanopores to approach the composition in the bulk phase – making the nanopores act as volumetric storage units at high pressures. However, there is still a substantial presence of heavy hydrocarbon molecules in the nanopores, making the overall fluid density in the nanopores high at high reservoir pressures. Essentially, at extreme overpressure, the organic nanopores act as volumetric storage units, holding significant amounts of compressed hydrocarbons.

Upon production from the reservoir at these high-pressure values, more of these compressed hydrocarbons are produced first at the expense of the heavy adsorbed ones. This is due to the attraction of the heavy hydrocarbon molecules to the nanopore walls – as the 'free' lighter hydrocarbon molecules are released, the heavy hydrocarbon molecules remain adsorbed, causing the overall viscosity of the remaining fluids in the nanopore to increase. (Bui and Akkutlu, 2017).

This state of volumetric storage in over-pressured reservoirs is likely to impact the production behavior from the formation during the pressure depletion. For example, by maintaining a light average fluid composition in the nanopore, it is possible that the compressed fluids in nanopores prevent capillary condensation and, even when capillary condensation occurs, the compressed fluid may cause a shift in the vaporization pressure. Additionally, gas expansion – not desorption – could stay as the dominant mechanism of production for a large range of pressure drawdown in these nanopores. In summary, rather than act as sites of heavy and trapped hydrocarbons, the nanopores could contribute to the

total recovery (via expansion) along with the bulk phase. This hypothesis will be tested based on the other results garnered in this study.

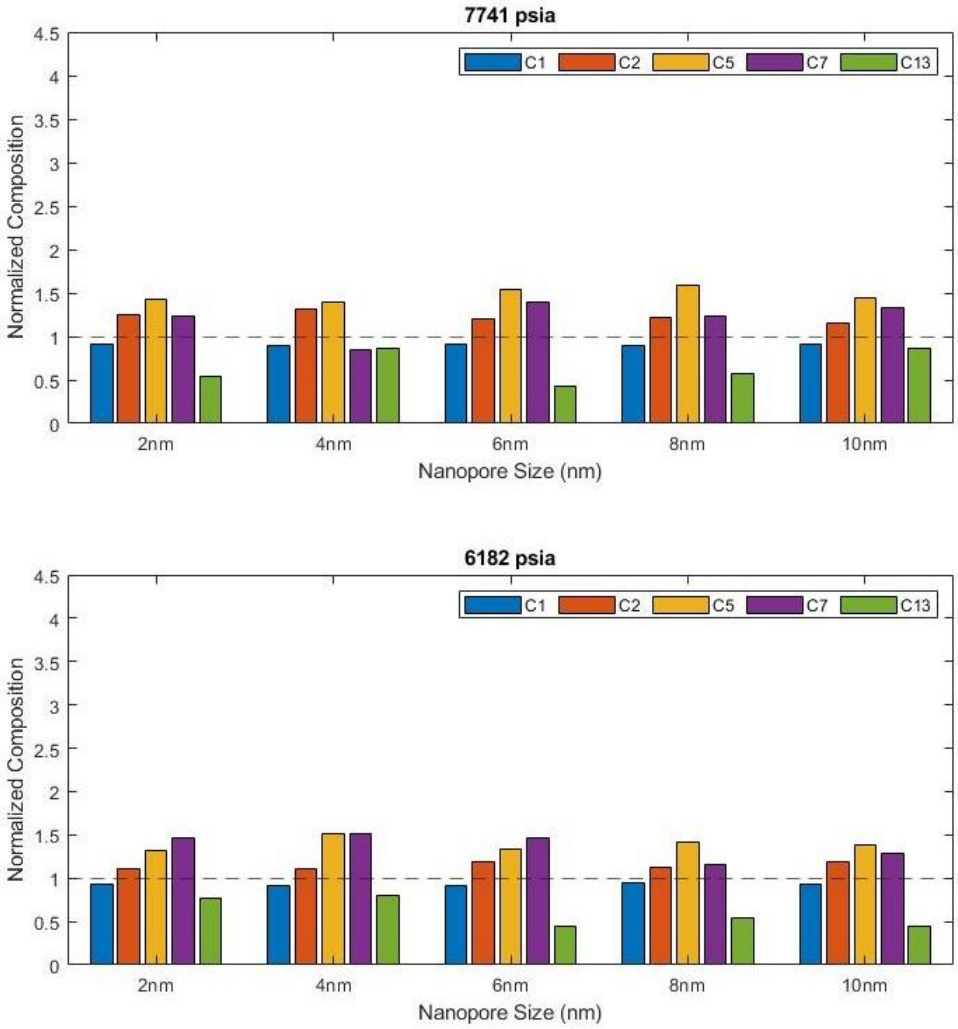

Figure 4.1. Normalized Pore Composition at High Reservoir Pressures. Nanoconfinement not Observed

In this study, production from the reservoir is simulated as pressure drawdown in the tanks. The nanopore, exposed to an initial pressure of 7,741 psia, is subjected to a pressure decrease in discreet values. During the corresponding fluid depletion, the behavior in the nanopore shifts from the state of volumetric storage to storage under

nanoconfinement effect. The nanoconfinement effect is first detected in the 2 nm pore (the smallest pore investigated) at around 4,674 psia (approximately 1,500 psia above the dew point pressure of the same mixture as the bulk fluid). At this pressure (see Figure 4.2.), so much of the lighter hydrocarbon molecules have been produced (relative to the heavy hydrocarbons) that the C13 molecules left in the 2 nm pore has a composition 2 times more than its composition in the produced bulk fluid. In the same pore, the more intermediate (C5 and C7) hydrocarbons have a composition 1.5 times more. At this pressure, and as the pore size is increased, the normalized pore composition approaches unity for all the fluid components, indicating volumetric storage. The fluid in the 10 nm pore essentially has the same composition as the fluid in the bulk phase.

At pressure values below the dew point pressure of the bulk fluid (see **Figure 4.3.**), the nanoconfinement is dominant, extending its effects into fluids in the larger pores. Just below the dew point pressure of the produced fluid composition in the bulk phase (2,882 psia), the fluid in the nanopores were C_{13}-rich – the fluid in the 2nm pore had as much as 3 times more C_{13} than in the produced fluid. As is to be expected with nanoconfinement, the normalized composition for C_{13} decreased with increase in pore size, while the normalized composition of the lighter hydrocarbons slightly increased with pore size.

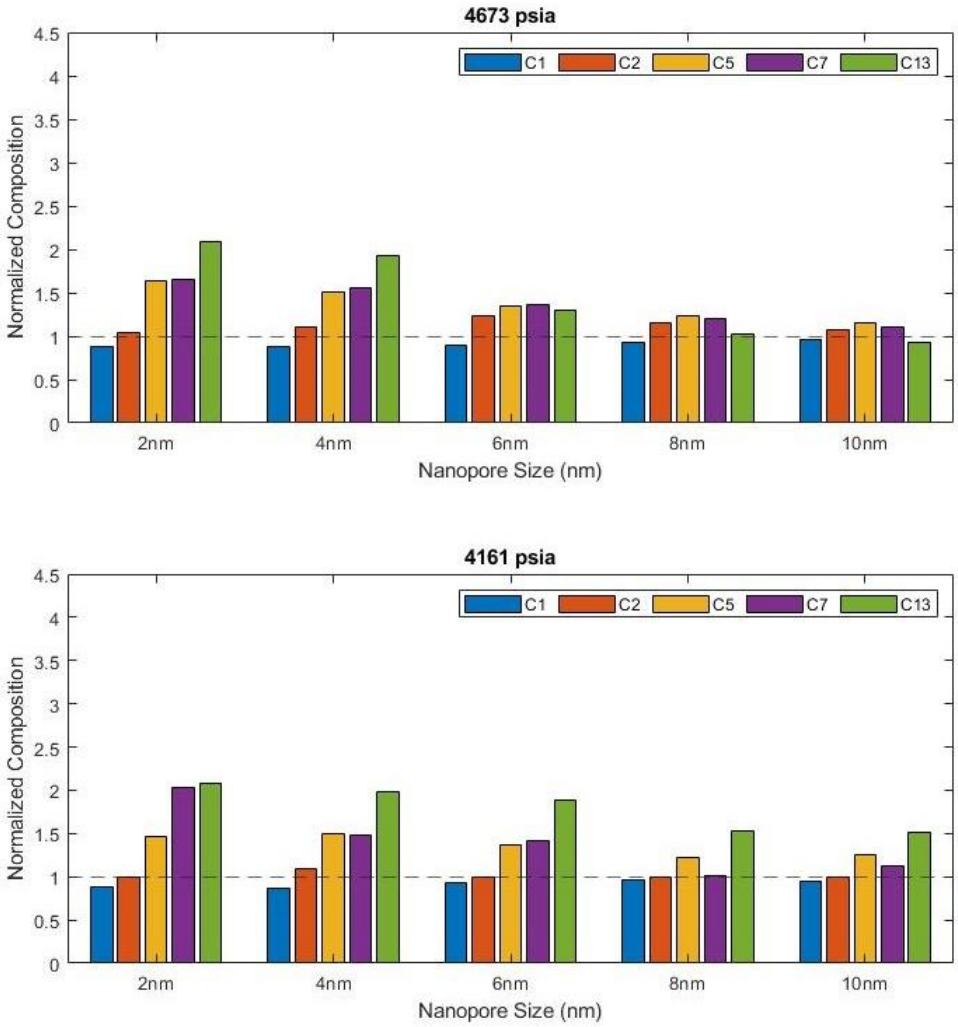

Figure 4.2. Normalized Average Fluid Composition in Nanopores during Fluid Depletion (Nanoconfinement Observed)

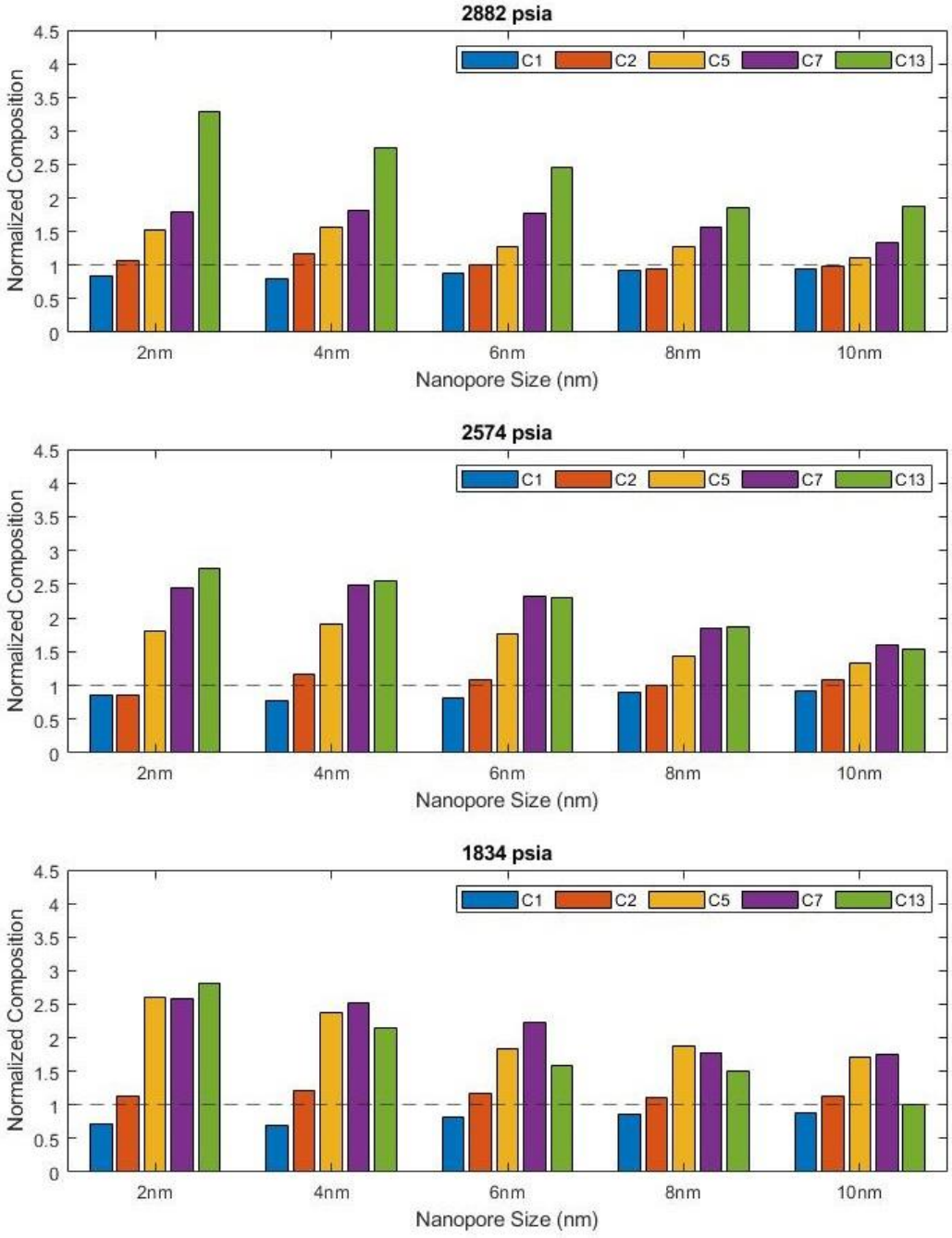

Figure 4.3. Normalized Pore Compositions at Pressures Below the Dew Point Pressure of the Bulk Fluid (Nanoconfinement Observed)

4.2. Fluid Density

4.2.1. Estimation of the Cutoff Pore Size

After redistributing the produced fluid into the different nanopores at different pressures, the fluid density in the nanopores were computed, and compared with the density of the bulk fluid. Due to the nanoconfinement effect, the greatest difference in the density values were in the smallest nanopores. As the nanopore size increases, the average fluid density approaches the density of the fluid in the bulk phase. The nanopore size at which the contained fluid has the same density as the bulk fluid is the cutoff pore size ($d_{p,L}$). Above this pore size, the nanoconfinement effects are minimal / non-existent.

Figure 4.4. shows how the fluid density varied by pore size at high reservoir pressures. The dashed line in the plots show the bulk density of the fluid at that pressure. The figure indicates that at 7742 psia and 6182 psia, the difference between the density of the fluid in the nanopore and the in bulk phase diminishes from the 8 nm pore (less than 8% difference). At these high pressures, the fluid in the 2 nm pore is less than 2 times denser than the produced fluid, and less than 1.1 times denser in the 10 nm pore.

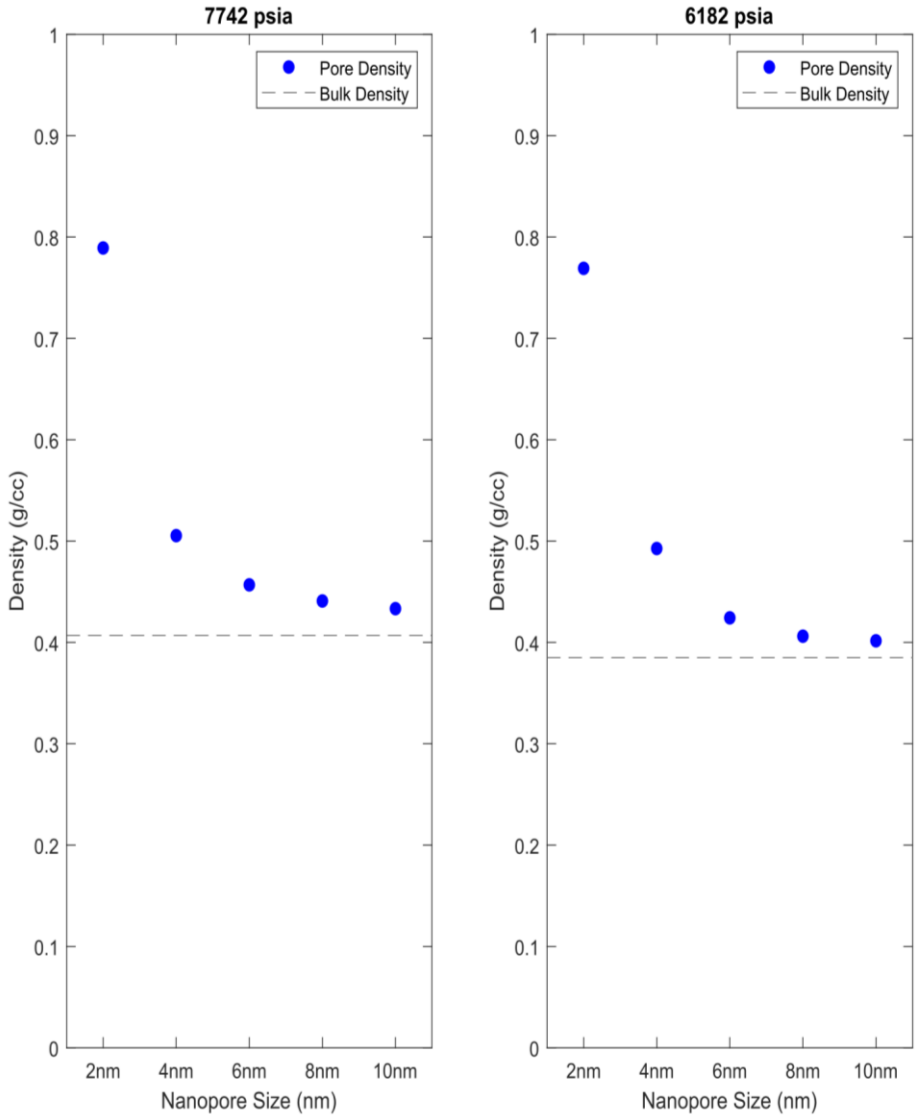

Figure 4.4. Density-Pore Size Plots at High Pressures

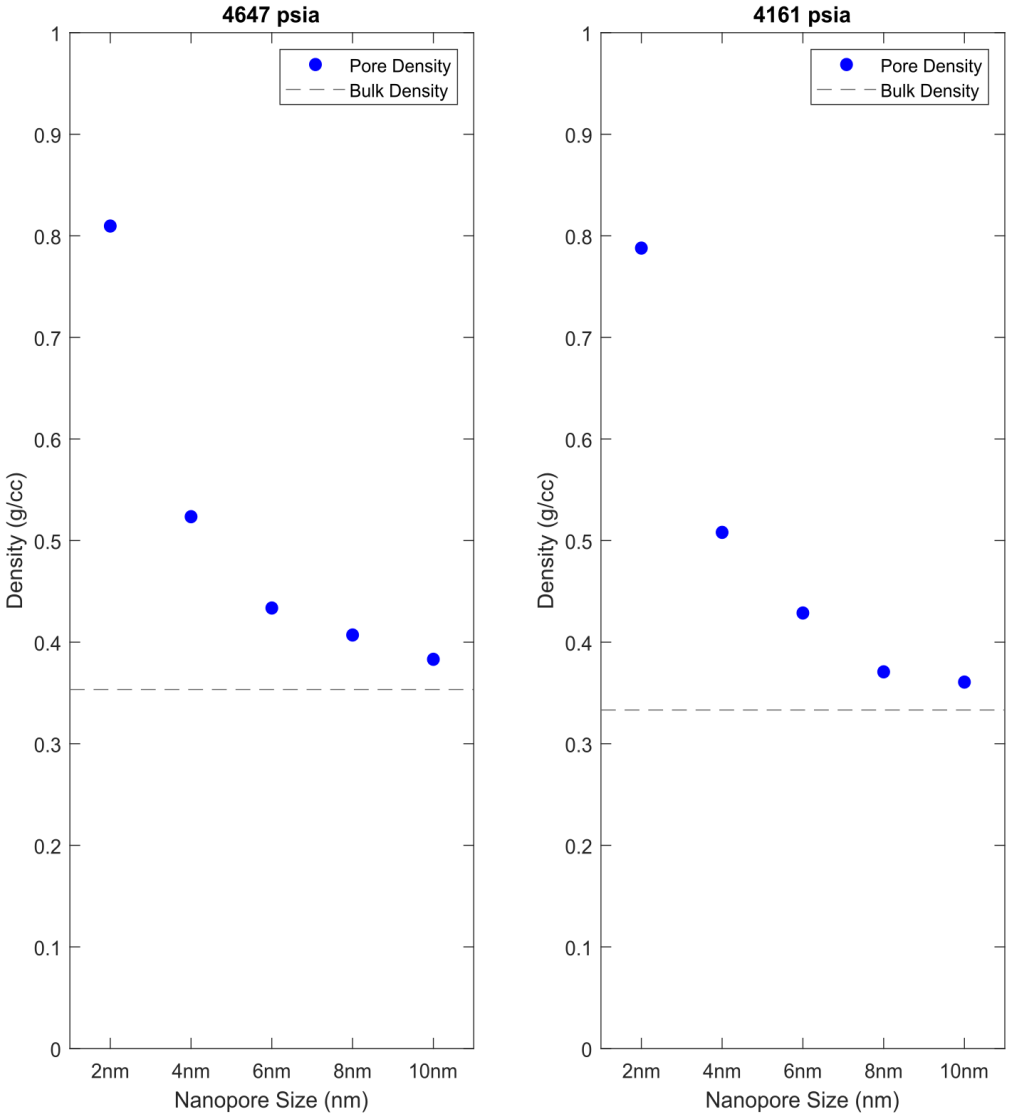

Figure 4.5. Density-Pore Size Plots at Lower Pressures After Fluid Depletion

At 4674 psia (where nanoconfinement is first observed), the influence of nanoconfinement on fluid density diminishes from the 10 nm pore (8% difference). Due to nanoconfinement effects, however, the density of the fluid in the 2 nm pore is more than 2 times more than that in the bulk fluid (see **Figure 4.5.**). At lower pressures (**Figure 4.6.**), the influence of nanoconfinement becomes minimal at 10 nm, but the fluid in the

nanopores become much denser than the bulk fluid. For instance, at 2575 psia, the fluid in the 2 nm pore is about 3 times denser than produced fluid, while it is about 4 times denser at 1834 psia.

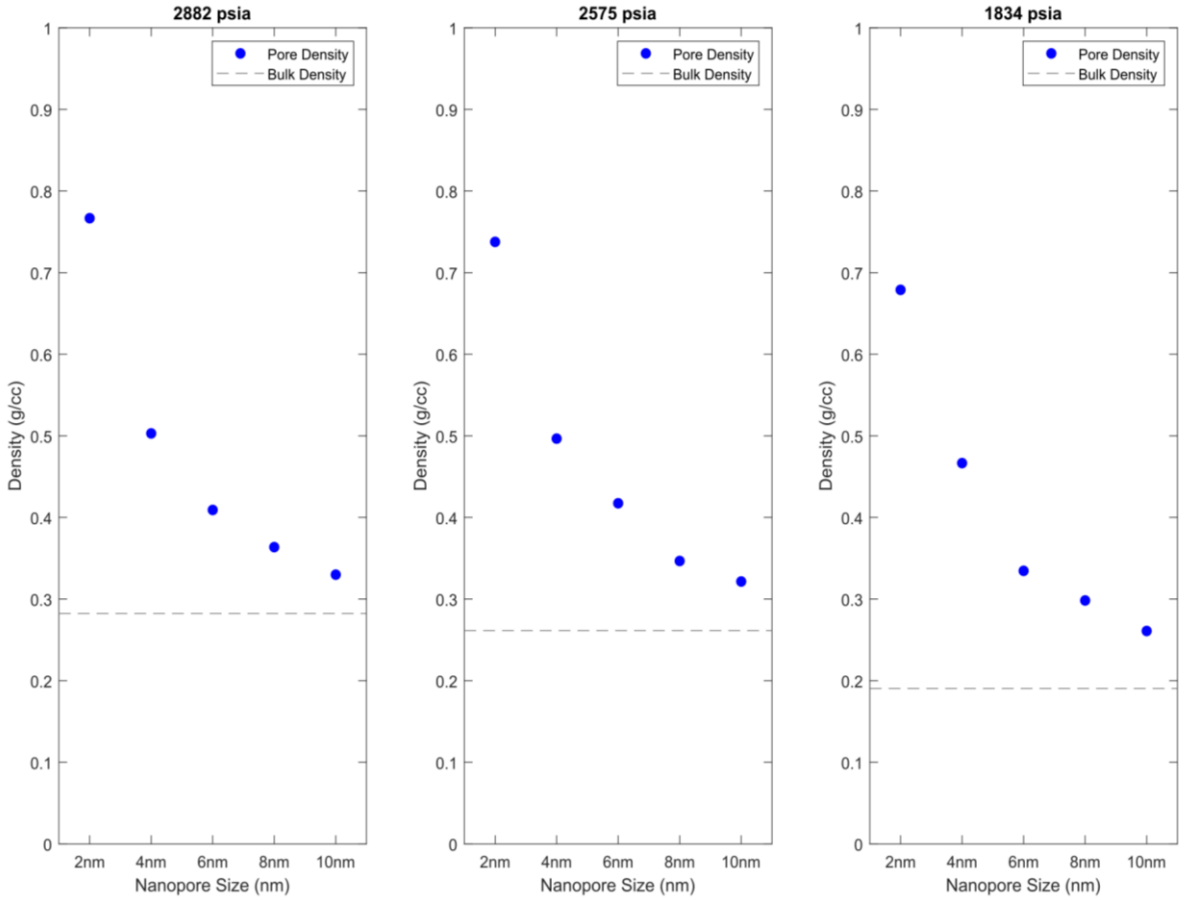

Figure 4.6. Density-Pore Size Plots at Pressures Below the Dew Point Pressure of the Bulk Fluid

4.2.2. Fluid Density with Pressure and the Estimation of Saturation Pressure

The influence of reservoir pressure on fluid density in the pores is consolidated in **Figure 4.7.** The fluid in the 2 nm pore across all pressure values is almost 2 times denser than the fluid in the 4 nm pore. The high density of the fluid in the 2 nm pore is a good indication of a high concentration of heavy hydrocarbons and the occurrence of capillary

condensation. The fluid density in the nanopores decreases with increase in pore size, until it reaches the bulk fluid density. The figure indicates that across all pressures (especially at the higher pressures), the fluid in the 10 nm pore was close in density to that of the bulk fluid – an indication that 10 nm is a good estimation of the cutoff pore size.

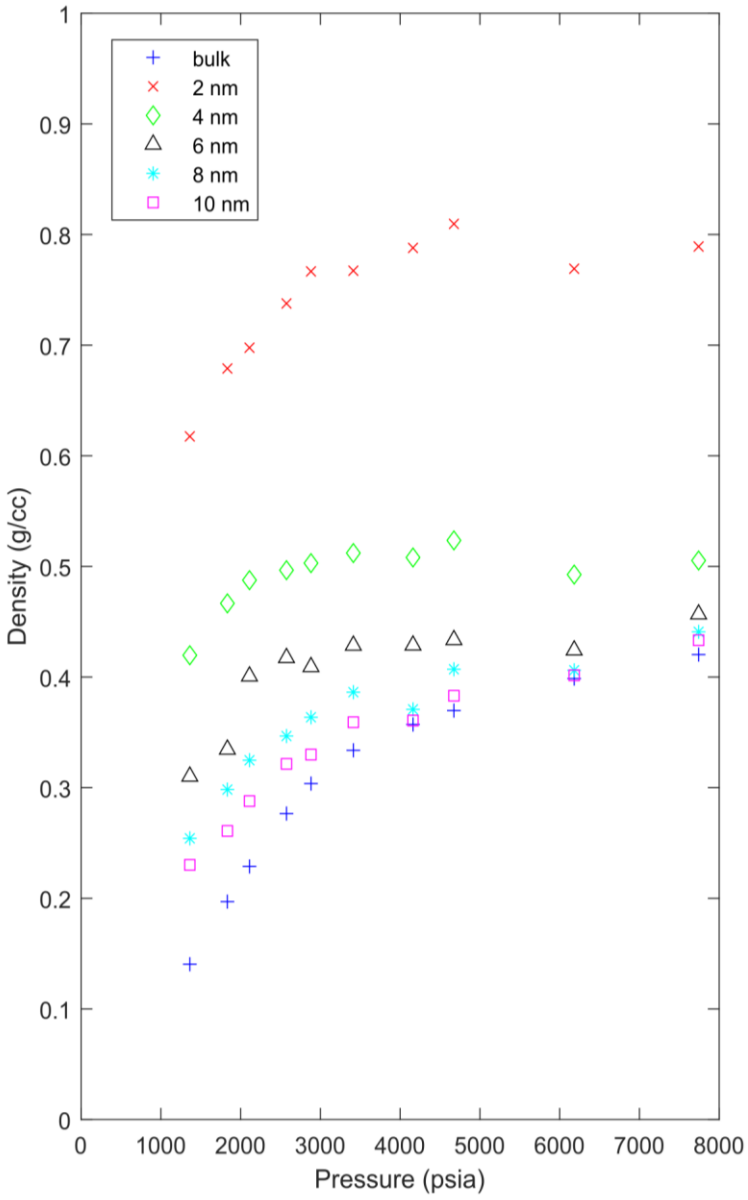

Figure 4.7. Density Variation with Pressure Across Different Nanopore Sizes

The density/pressure profile follows a similar trend across all the investigated nanopore sizes – at high pressures, the fluid density remained constant, but fell steeply below the fluid's saturation (dew or vaporization) point at that pressure and pore size. Below the saturation pressure, phase change instigates the rapid decline in density. Hence, the saturation pressure of the fluid in each of the nanopores can be estimated as the turning point of the fluid's density/pressure profile at that pore size. For instance, **Figure 4.8.** shows how the saturation (dew) point pressure of the bulk fluid was estimated to be 3071.1 psia.

Table 4.1. shows the estimated saturation pressure of the fluid in the different nanopore sizes. The table shows the influence of nanoconfinement on the saturation pressure. Generally, nanoconfinement effect decreased the saturation pressure of the fluid – this is observed between the 4 nm and 10 nm pores. Due to the similarity of the fluid composition in the 10 nm pore and the bulk phase, the saturation pressures are nearly equal (2.3% difference).

The fluid in the 2 nm pore has a saturation point comparable to that of the fluid in the bulk phase. As seen in **Figure 4.7.**, this may be due to the high density of the fluid relative to the bulk fluid. It is also another good indication of the occurrence of capillary condensation in that pore size. At the larger pore sizes (6 – 10 nm pores), however, it can be surmised from **Figure 4.7.** that, although the fluids in these pores are denser than in the bulk phase (due to the higher presence of heavy hydrocarbons), capillary condensation does not occur in these pores – the fluids remain as vapor (just as in the bulk phase) at high pressures, with liquid dropping out below the fluid's dew point at that pore size.

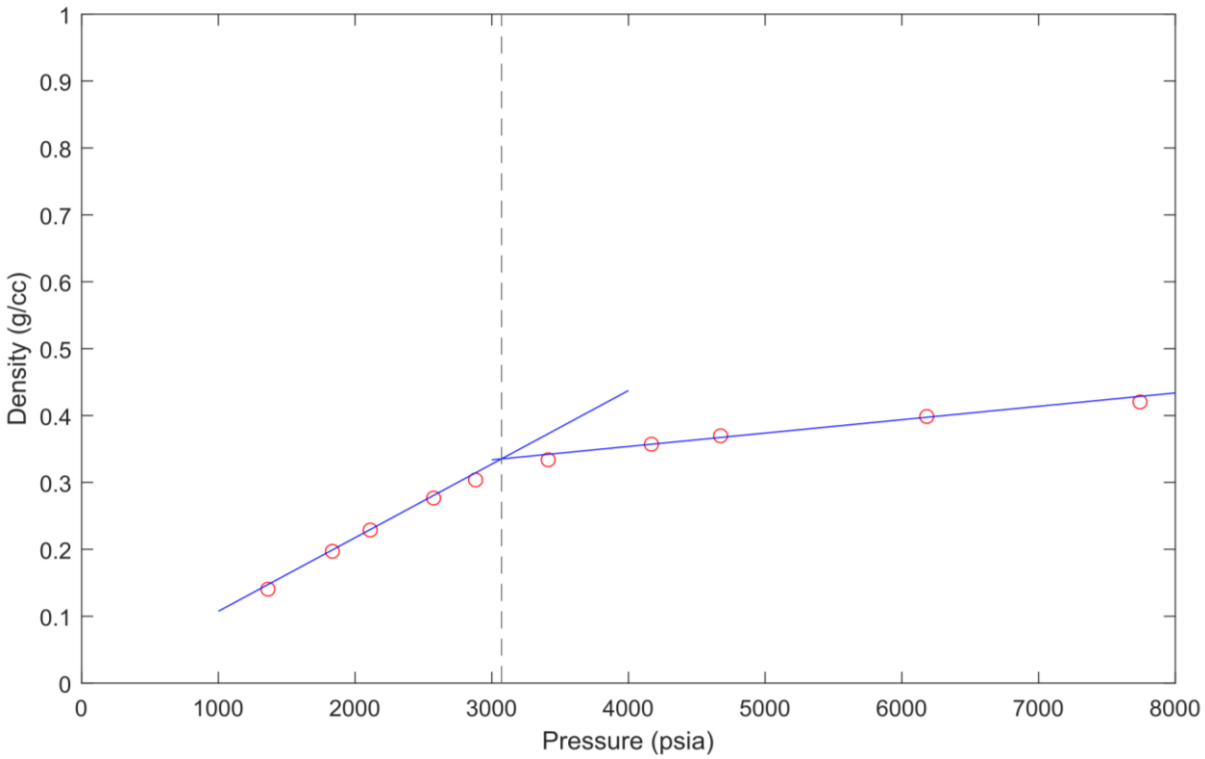

Figure 4.8. Estimating the Dew Point Pressure of the Bulk Fluid

Table 4.1. Saturation Pressure of the Recombined Fluid Composition

Pore Size (nm)	**Saturation Pressure (psia)**
2	3001.1
4	2341.1
6	2372.0
8	2783.3
10	2998.1
Bulk	3071.1

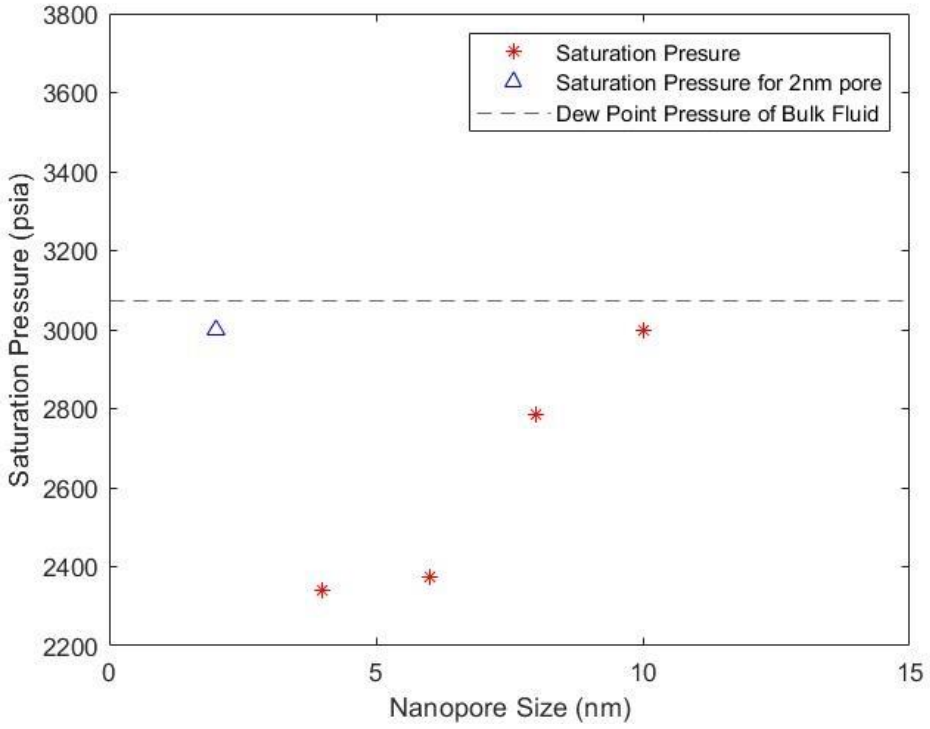

Figure 4.9. Saturation Pressure of Pore Fluids

4.3. Fluid Recovery from the Nanopores

The recovery from an individual nanopore was computed as the difference between the gas-in-place (in that nanopore) at an initial pressure of approximately 8000 psia, and the gas-in-place at a pressure of interest. The results are expressed as percentages in **Figure 4.10.**

As discussed by Baek and Akkutlu (2019a), the plot can be separated into two regions – a region of low recovery (recovery by desorption of adsorbed gases in small nanopores), and a region of high recovery (recovery by expansion of the gas in the bulk phase and large pores). **Figure 4.10.**, however, shows that the recovery of the fluid via expansion at high pressures (above the dew point pressure) from the bulk phase is

comparable to the fluid recovered via ‘desorption’ from the small nanopores. A potential explanation for this is that as the pressure of the system is gradually reduced from the initial high pressure, the excess light hydrocarbons in the small pores ‘expand’, and are produced – little or no desorption of the heavy hydrocarbons in the small nanopores occurs at this stage.

As the pressure reduces, and nanoconfinement is observed in the pores, the hydrocarbon recovery from the large pores (bulk phase) is magnitudes greater than the production from the low-recovery desorption region. As seen in the figure, below the dew point pressure, the recovery at 1336 psia from the individual pores in the bulk phase is about 70%. From the 2 nm pore, however, fluid recovery is only 48%.

4.4. Optimization of Fluid Production from Organic-Rich Source Rocks in the Presence of Nanoconfinement Effects

As earlier discussed, and as shown in **Figure 4.10.**, the amount of fluids recovered from the source rock depends largely on the initial pressure of the reservoir, the production pressure, and the pore-size distribution of the reservoir. If the initial reservoir pressure is high such that nanoconfinement effects are minimized or eliminated, and the pressure draw-down is small such that nanoconfinement effect on production is still negligible, the recovery from the nanopores (pore size generally equal to or smaller than 10 nm) is comparable to the recovery from the bulk phase (pore size greater than 10 nm). The 10 nm pore is considered as the threshold (cut-off) pore size in this study due to the minimal effects of nanoconfinement in pores with sizes greater than 10 nm. (See **Figures 4.4.** – **4.6.**).

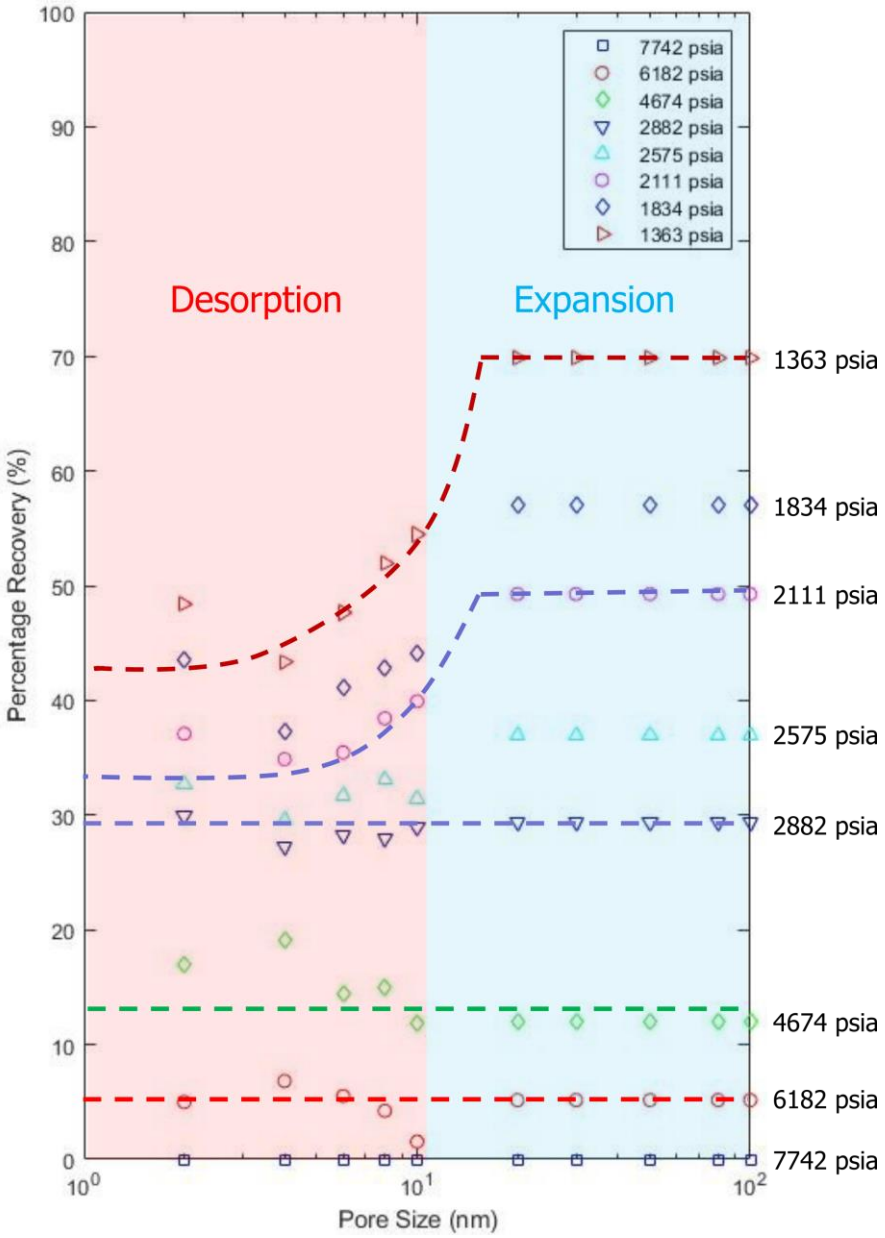

Figure 4.10. Fluid Recovery from Nanopores

Baek and Akkutlu (2019c) showed that, under nanoconfinement effects, the gas-in-place (in scf/ton) at a pressure p is given as:

$$G^*(p) = 1.2603 \times 10^6 \times V_p \times \left(\nu \times n_b + \sum_{d_p}^{d_{p,L}} \frac{V_{\%,d_p}}{100} \times n_{d_p}\right) \quad \text{..... (40)}$$

The first term in the parenthesis in equation (40) represents the fluids in the bulk phase (including the pores with sizes greater than the cut-off $d_{p,L}$), while the second term represents the nanoconfined fluid in the pores with sizes smaller than the cut-off. V_p is the effective hydrocarbon pore volume in cm^3/g, expressed as $\phi(1 - s_w)/\rho_b$. n_b the number of molecules per cubic Angstrom pore volume making up the bulk fluid, and n_{d_p} the number of molecules of the fluid in the pore of size d_p.

In order to proceed with the hydrocarbon-in-place calculations using equation (40), two hypothetical rock samples (Sample 1 and Sample 2) were considered, from Baek and Akkutlu, 2019c. The pore size distributions of these rock samples and their reservoir properties are given in **Figure 4.11.** and **Table 4.2.** respectively, Sample 1 has a significant number of small pores below the cut-off pore size of 10 nm, while Sample 2 has more of the large pores holding up the fluid in the bulk phase. To simplify the calculations, both samples were assumed to come from the similar reservoirs, whose properties are shown in **Table 4.2.**

At the initial reservoir pressure of approximately 8000 psia, and at temperature of 107°F, the number density (in mol/Å^3) of the fluid molecules in each pore size present in the reservoir are given in **Table 4.3.** For the pores smaller than or equal to the cut-off size of 10 nm, the number density was computed via the results of the molecular simulation in the nanopore at equilibrium. For pores in the bulk phase, the number density was computed by averaging the number of molecules in the tanks at equilibrium.

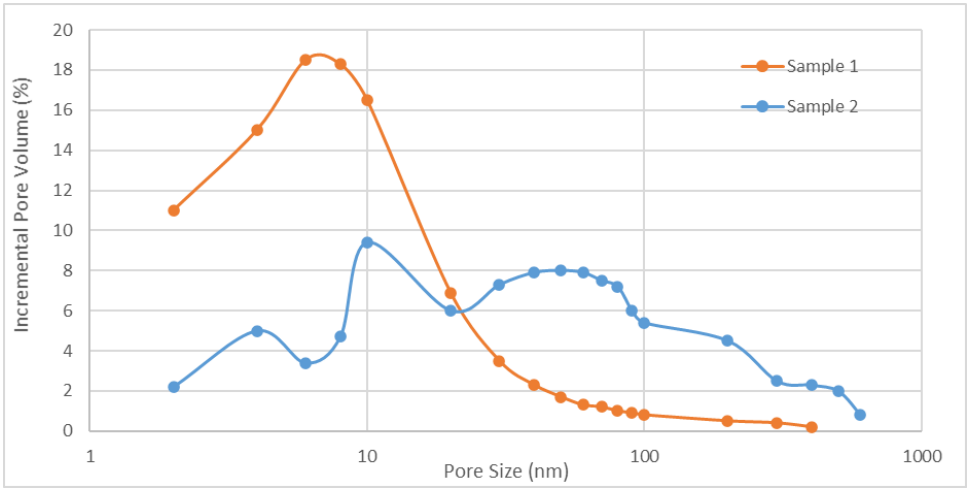

Figure 4.11. Pore Size Distribution of two Organic-Rich Shale Samples. Adopted from Baek and Akkutlu (2019c).

Table 4.2. Reservoir Properties (Baek and Akkutlu, 2019c).

Rock Property	**Value**	**Unit**
Bulk density (ρ_b)	2.5	g/cm^3
Total porosity (ϕ)	5	%
Immobile water saturation (s_w)	35	%

Table 4.3. Number Density of Fluid in Pores by Pore Size

Nanopore Size (Å)	**Number density (mol/Å^3)**
20	0.0139803
40	0.009763501
60	0.009084403
80	0.008532543
100	0.008326454
>100	0.008704425

Adopting equation (40), the cumulative hydrocarbon in place (in scf/ton) for the reservoirs, from which Samples 1 and 2 are taken, are shown in **Figure 4.12.** by pore size. It is estimated that the samples hold between 140 – 160 scf/ton of condensate gas at the initial pressure. In addition, due to the significant presence of nanopores in Sample 1, these small nanopores contribute considerably to the hydrocarbon in place. The reverse is the case of Sample 2, where the bulk phase contributes more to the hydrocarbon in place.

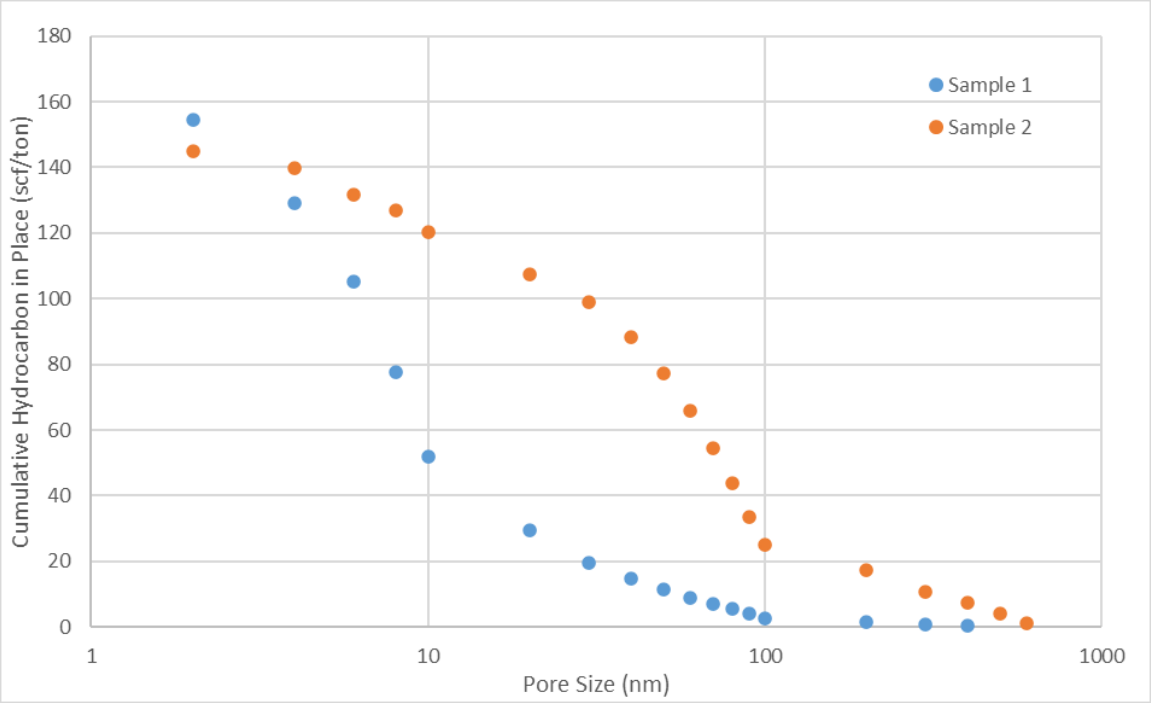

Figure 4.12. Cumulative Hydrocarbon in Place by Pore Size for Samples 1 and 2.

Figure 4.13. and **Figure 4.14.** show the amount of hydrocarbons recovered per ton of rock as a function of pore size and pressure for Rock Sample 1 and 2, respectively.

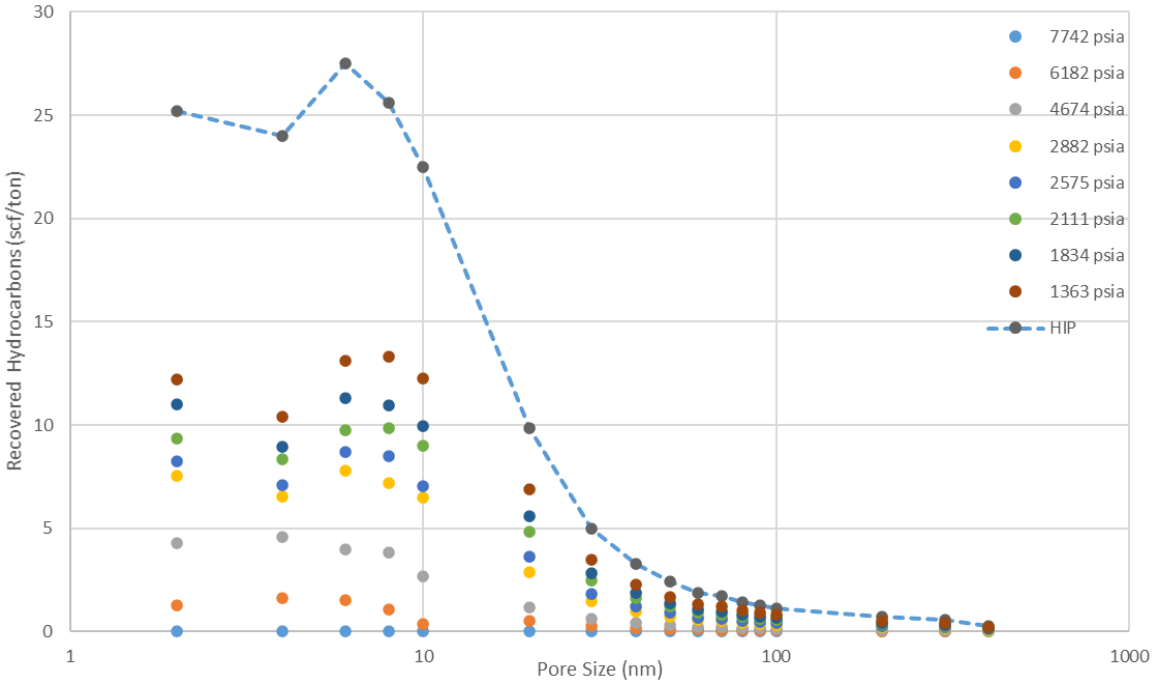

Figure 4.13. Incremental Amount of Hydrocarbons Recovered from Sample 1 as a Function of Pressure and Pore Size

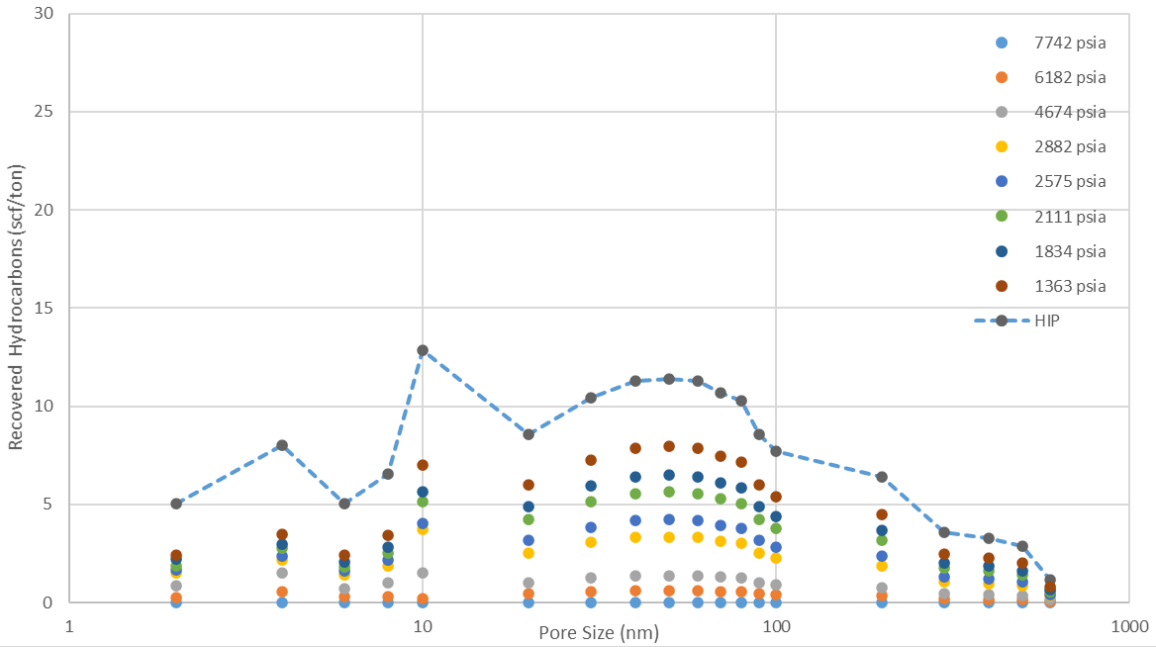

Figure 4.14. Incremental Amount of Hydrocarbons Recovered from Sample 2 as a Function of Pressure and Pore Size

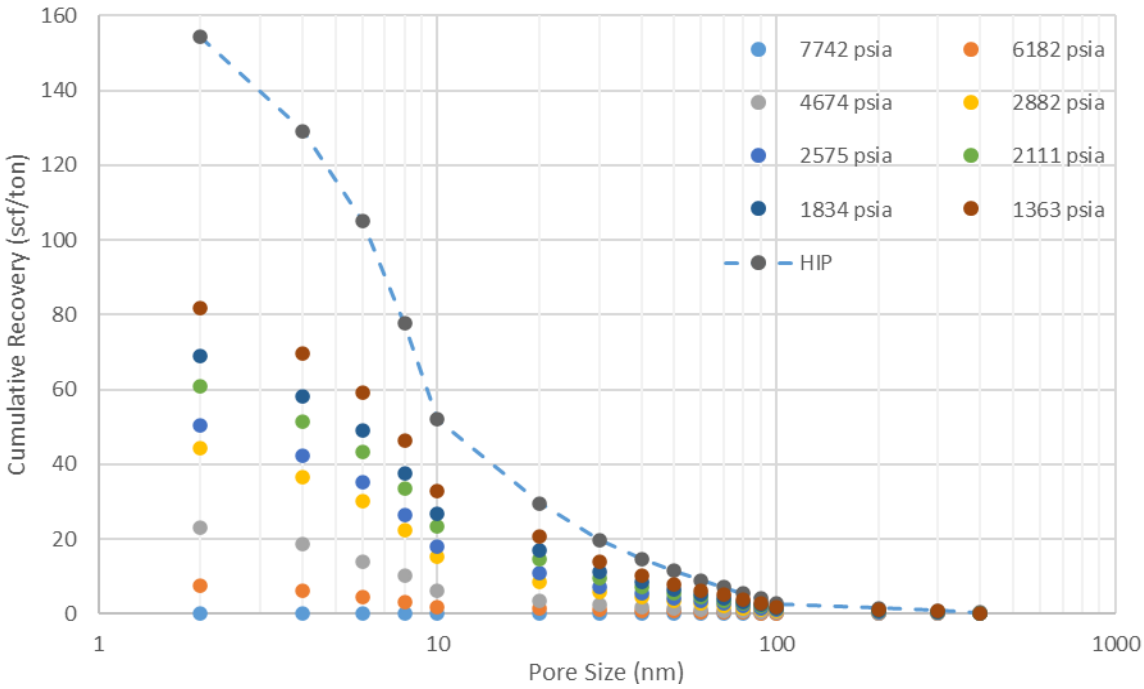

Figure 4.15. Cumulative Amount of Hydrocarbons Recovered from Sample 1 as a Function of Pressure and Pore Size

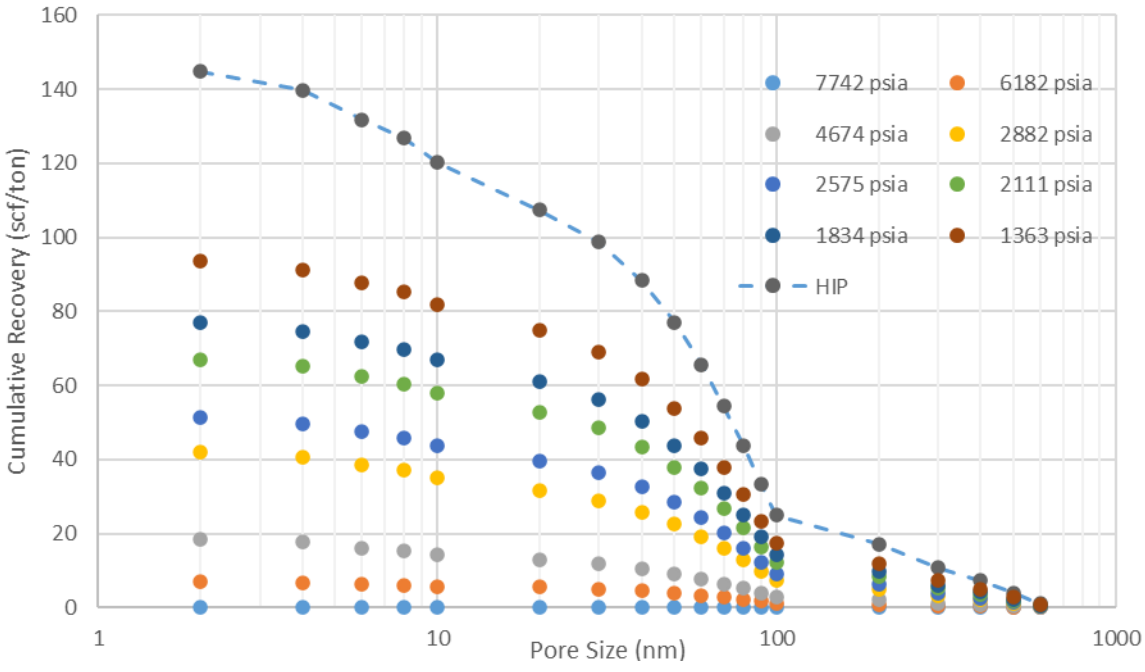

Figure 4.16. Cumulative Amount of Hydrocarbons Recovered from Sample 2 as a Function of Pressure and Pore Size

The dashed line in **Figure 4.13.** and **4.14.** shows the total initial volume of hydrocarbons in-place contained in each pore. For instance, Sample 1 in **Figure 4.13.**, has 25 scf initial volume of hydrocarbons in the 2 nm pore (at 7742 psia) per ton of rock. At this initial reservoir pressure, no hydrocarbons have been recovered from the reservoir yet. As the reservoir pressure is reduced, the volume of hydrocarbons recovered from each of the available pores are represented by the isobaric profiles shown as circular data points in the figure. Similarly, **Figure 4.14.** gives the recovery data for Sample 2. **Figure 4.15.** and **4.16.** show the same recovery information on a cumulative scale for Sample 1 and 2 respectively.

Figure 4.10. shows that the effects of nanoconfinement on the amount of fluid recovered became apparent at approximately 2575 psia. Below this pressure, the difference in the amount of fluids recovered via adsorption and expansion become exaggerated. However, **Figure 4.13.** and **Figure 4.14** highlight the importance of having and understanding the pore size distribution of the reservoir in order to understand and optimize production. For reservoirs with a high proportion of small pores (as illustrated by Rock Sample 1), **Figure 4.13.** shows that, compared to the amount of hydrocarbons recovered from the large pores, significant amounts of hydrocarbons can still be recovered from the small pores via desorption below 2575 psia. However, for reservoirs with a high proportion of large pores (as illustrated by Rock Sample 2), producing below 2575 psia does not significantly contribute to fluid desorption in the small pores. (See **Figure 4.14.**). Since the gas in the large pores can be produced via expansion, production in this kind of reservoir can be optimized by maintaining a relatively high bottomhole pressure.

5. CONCLUSIONS

In this investigation of nanoconfinement of a condensate fluid in an over-pressured reservoir, the study revealed that although the fluid at high pressures (generally greater than 6000 psia) are denser than the fluids in the bulk phase, nanoconfinement effects at these pressures are minimal. Essentially, the fluids in the nanopores and the bulk phase have the same composition, as indicated by the normalized pore composition of each of the components, which is close to unity.

Nanoconfinement effects are first observed at lower pressures (around 5000 psia). At these pressures, the heavy hydrocarbon components are consistently magnitudes higher in concentration than the lighter components in small nanopores. These nanoconfinement effects reduce with increase in pore size and diminishes at a cut-off pore size, which was estimated to be 10 nm in this study. At this pore size, the fluid density is comparable to that of the bulk fluid.

Across all investigated pressures, the density of the fluid in the small nanopores were consistently higher than that in the bigger nanopores and the bulk phase. For instance, in this study, the fluid in the 2 nm pore was 1.5 times denser than the fluid in the 4 nm pore, and more than 2 times denser than the fluid in the bulk phase. The high fluid density in the 2 nm pore is an indication of the occurrence of capillary condensation.

This study also showed the effects of nanoconfinement on the dew point pressure of the fluid in the pores. As the pore size increases (that is, nanoconfinement reduces), the dew point pressure increased until the dew point pressure in the bulk phase. In this study,

the dew point pressure increased from 2341.1 psia in the 4 nm pore, to 3071.1 psia in the bulk phase. The dew point pressure in the 2 nm pore was, however, comparable to that in the bulk phase. Although the conclusion is that this is due to the high density of the fluid in this pore, this phenomenon can be further researched.

REFERENCES

Akkutlu, I. Y., & Fathi, E. (2012). Multiscale gas transport in Shales with Local Kerogen Heterogeneities. *SPE Journal*, *17*(04), 1002–1011. https://doi.org/10.2118/146422-pa

Al Ismail, M. I., & Horne, R. N. (2014). Modeling Adsorption of Gases in Nanoscale Pores Using Grand Canonical Monte Carlo Simulation Techniques. *SPE Journal*. https://doi.org/10.2118/170948-ms

Ambrose, R. J., Hartman, R. C., & Akkutlu, I. Y. (2011). Multi-component Sorbed-phase Considerations for Shale Gas-in-place Calculations. *SPE Journal*, 1–9. https://doi.org/10.2118/141416-ms

Ambrose, R. J., Hartman, R. C., Diaz-Campos, M., Akkutlu, I. Y., & Sondergeld, C. H. (2012). Shale Gas-in-Place Calculations Part I: New Pore-Scale Considerations. *SPE Journal*, *17*(1), 219–229. https://doi.org/10.2118/131772-pa

Arthur, M. A., & Sageman, B. B. (1994). Marine Black Shales: Depositional Mechanisms and Environments of Ancient Deposits. *Annual Review of Earth and Planetary Sciences*, *22*(1), 499–551. https://doi.org/10.1146/annurev.ea.22.050194.002435

Baek, S., & Akkutlu, I. Y. (2019). CO_2 Stripping of Kerogen Condensates in Source Rocks. *SPE Journal*, *24*(03), 1415–1434. https://doi.org/10.2118/190821-pa

Baek, S., & Akkutlu, I. Y. (2019). Mean Free Path of Gas Molecules in Organic Nanochannels Using Molecular Simulations. *SPE Journal*, *24*(06), 2555–2573. https://doi.org/10.2118/198889-pa

Baek, S., & Akkutlu, I. Y. (2019). Produced-Fluid Composition Redistribution in Source Rocks for Hydrocarbon-In-Place and Thermodynamic Recovery Calculations. *SPE Journal*, *24*(03), 1395–1414. https://doi.org/10.2118/195578-pa

Balbuena, P. B., & Seminario, J. M. (1999). *Molecular Dynamics: From Classical to Quantum Methods*. Elsevier.

Bui, K., & Akkutlu, I. Y. (2016). Hydrocarbons Recovery from Model-Kerogen Nanopores. *SPE Journal*, *22*(03), 854–862. https://doi.org/10.2118/185162-pa

Chen, J.-H., Mehmani, A., Li, B., Georgi, D., & Jin, G. (2013). Estimation of Total Hydrocarbon in the Presence of Capillary Condensation for Unconventional Shale Reservoirs. *SPE Journal*. https://doi.org/10.2118/164468-ms

Danesh, A. (Ed.). (2007). *PVT and Phase Behaviour of Petroleum Reservoir Fluids*. Elsevier.

Das, M., Jonk, R., & Schelble, R. (2012). Effect of Multicomponent Adsorption/Desorption Behavior on Gas-In-Place (GIP) Calculations and Estimation of Free and Adsorbed CH_4 and CO_2 in Shale Gas Systems. *SPE Journal*. https://doi.org/10.2118/159558-ms

Diaz Campos, M. (2010), Uncertainties in Shale Gas In-place Calculations: Molecular Simulation Approach. M.S. Thesis in Petroleum Engineering, the University of Oklahoma.

Didar, B. R., & Akkutlu, I. Y. (2015). Confinement Effects on Hydrocarbon Mixture Phase Behavior in Organic Nanopore. *Unconventional Resources Technology Conference*. https://doi.org/10.2118/178519-ms

Feng, F., & Akkutlu, I. Y. (2015). Flow of hydrocarbons In Nanocapillary: A Non-equilibrium Molecular Dynamics Study. *SPE Journal*. https://doi.org/10.2118/177005-ms

Frenkel, D., & Smit, B. (2002). *Understanding Molecular Simulation: From Algorithms to Applications* (2nd ed., Vol. 1, Ser. Computational Science Series). Academic Press.

Gonzalez, M. A. (2011). *Force Fields and Molecular Dynamics Simulations*. Neutron Sciences. Retrieved September 12, 2021, from https://www.neutron-sciences.org/articles/sfn/pdf/2011/01/sfn201112009.pdf.

Haile, J. M. (1992). *Molecular Dynamics Simulation: Elementary Methods*. Wiley.

Ilgen, A. G., Heath, J. E., Akkutlu, I. Y., Bryndzia, L. T., Cole, D. R., Kharaka, Y. K., Kneafsey, T. J., Milliken, K. L., Pyrak-Nolte, L. J., & Suarez-Rivera, R. (2017). Shales at all scales: Exploring Coupled Processes in Mudrocks. *Earth-Science Reviews, 166*, 132–152. https://doi.org/10.1016/j.earscirev.2016.12.013

Kou, R., Alafnan, S. F., & Akkutlu, I. Y. (2016). Multi-scale Analysis of Gas Transport Mechanisms in Kerogen. *Transport in Porous Media*, *116*(2), 493–519. https://doi.org/10.1007/s11242-016-0787-7

Li, D., Zhang, L., Wang, J. Y., & Lu, D. (2016). Composition-Transient Analysis in Shale-Gas Reservoirs with Consideration of Multicomponent Adsorption. *SPE Journal*, *21*(02), 648–664. https://doi.org/10.2118/178435-pa

Loucks, R. G., Reed, R. M., Ruppel, S. C., & Hammes, U. (2012). Spectrum of Pore Types and Networks in Mudrocks and a Descriptive Classification for Matrix-Related Mudrock Pores. *AAPG Bulletin, 96*(6), 1071–1098.

Loucks, R. G., Reed, R. M., Ruppel, S. C., & Jarvie, D. M. (2009). Morphology, Genesis, and distribution of Nanometer-Scale pores In Siliceous mudstones of the Mississippian Barnett Shale. *Journal of Sedimentary Research*, *79*(12), 848–861. https://doi.org/10.2110/jsr.2009.092

Mackay, D. H., Cross, A. J., & Hagler, A. T. (1989). The Role of Energy Minimization in Simulation Strategies of Biomolecular Systems. *Prediction of Protein Structure and the Principles of Protein Conformation*, 317–358. https://doi.org/10.1007/978-1-4613-1571-1_7

Martin, M. G., & Siepmann, J. I. (1998). Transferable Potentials for Phase Equilibria. 1. United-atom Description of n-alkanes. *The Journal of Physical Chemistry B*, *102*(14), 2569–2577. https://doi.org/10.1021/jp972543+

McCain, W. D. (2017). *The Properties of Petroleum Fluids*. PennWell.

Péneloux, A., Rauzy, E., & Fréze, R. (1982). A Consistent Correction for Redlich-Kwong-Soave Volumes. *Fluid Phase Equilibria*, *8*(1), 7–23. https://doi.org/10.1016/0378-3812(82)80002-2

Peng, D.-Y., & Robinson, D. B. (1976). A New Two-Constant Equation of State. *Industrial & Engineering Chemistry Fundamentals*, *15*(1), 59–64. https://doi.org/10.1021/i160057a011

Pitakbunkate, T., Balbuena, P. B., Moridis, G. J., & Blasingame, T. A. (2016). Effect of Confinement on Pressure/ Volume/Temperature Properties of Hydrocarbons in Shale Reservoirs. *SPE Journal*, *21*(02), 621–634. https://doi.org/10.2118/170685-pa

Potter, P. E., Maynard, J. B., & Depetris, P. J. (2005). *Mud and Mudstones: Introduction and Overview*. Springer.

Rapaport, D. C. (2004). *The Art of Molecular Dynamics Simulation* (2nd ed.). Cambridge University Press.

Rezaee, R. (Ed.). (2015). *Fundamentals of Gas Shale Reservoirs*. John Wiley & Sons.

Riewchotisakul, S., & Akkutlu, I. Y. (2016). Adsorption-Enhanced Transport of Hydrocarbons in Organic Nanopores. *SPE Journal*, *21*(06), 1960–1969. https://doi.org/10.2118/175107-pa

Shah, M. S., Siepmann, J. I., & Tsapatsis, M. (2017). Transferable Potentials for Phase Equilibria. Improved United-Atom Description of Ethane and Ethylene. *AIChE Journal*, *63*(11), 5098–5110. https://doi.org/10.1002/aic.15816

Sharma, S. (Ed.). (2019). Molecular Dynamics Simulation of Nanocomposites Using BIOVIA Materials Studio, LAMMPS and GROMACS. https://doi.org/10.1016/b978-0-12-816954-4.00003-6

Tolbert, B. T., & Wu, X. (2015). Quantifying Pore Size Distribution Effect on Gas in Place and Recovery Using SLD-PR EOS for Multiple-Components Shale Gas Reservoir. *SPE Journal*. https://doi.org/10.2118/176992-ms

Tucker, M. E. (2001). *Sedimentary Petrology: An Introduction to the Origin of Sedimentary Rocks* (3rd ed.). Blackwell Publishing.